Article

Fast Method to Determine Solubility Products of Sparingly Soluble Salts by Combining Titration Experiments and Thermodynamic Modeling: A Case Study on the Example of Cu/Zn Based Catalyst Precursors and Ni/Mn Based Precursors for Cathode Active Material

Published as part of Industrial & Engineering Chemistry Research virtual special issue "Marco Mazzotti Festschrift".

David Guse,* Lukas Metzger, Martin Kriesten, Elisabeth Eiche, and Matthias Kind*
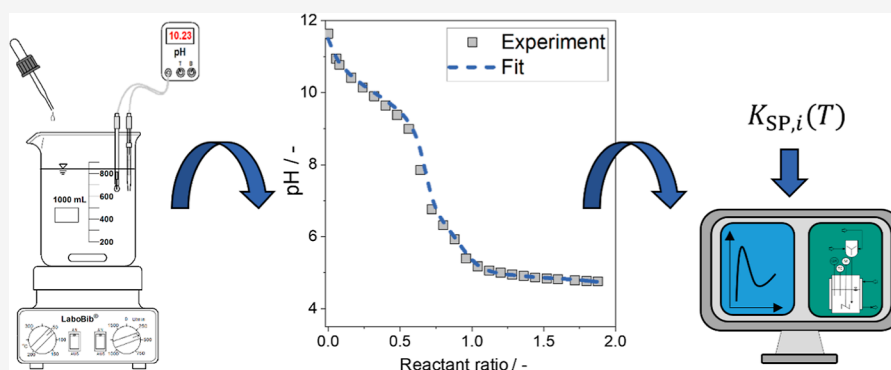
Read Online

ACCESS | Metrics & More | Article Recommendations | Supporting Information

ABSTRACT: Solubility products are essential for the thermodynamic and kinetic modeling of (co-)precipitation processes. However, due to the complexity in the determination of solubility products of sparingly soluble salts, models often rely on the limited data for minerals, which may differ in the elemental composition or crystallographic properties when compared to their synthetic counterparts. Thus, we developed an easily accessible method to determine solubility products for synthetic precipitate phases as a function of the temperature and elemental composition based on simple titration studies and a thermodynamic equilibrium model. By applying this method, we determined solubility products for the synthetic precursor phase zincian georgeite ($[Cu,Zn]_2CO_3(OH)_2$), which is relevant in the preparation of Cu/Zn-based catalysts, as a function of temperature and its Zn fraction. The data significantly differ from the data for the mineral rosasite ($Cu_{1.16}Zn_{0.84}CO_3(OH)_2$) which is used so far, and applying the new data resulted in an improved model accuracy. Furthermore, we identified $Ni_8(OH)_{14}SO_4$ as a phase that is possibly responsible for the incorporation of sulfate ions into the precursor for cathode active material (PCAM) and determined its solubility product. Using these results, we were able to predict the phase composition of Ni/Mn-based PCAM and the degree of sulfate incorporation as a function of pH. Both examples show the applicability and relevance of our method to determine solubility products for the modeling of industrial relevant (co-)precipitation processes.

1. INTRODUCTION

Precipitation and co-precipitation are key processes not only in the production of many economically significant particulate products, such as Cu/Zn-based catalysts for methanol synthesis[1] and precursors for the cathode active material (PCAM) in Li-ion batteries[2,3] and pigments,[4] but also in the water purification[5] or quantitative analysis.[6] On the one hand, the chemical industry has to become sustainable and as CO_2 neutral as possible in the future, but on the other hand, there is still increasing demand for high-quality products: for instance, the annual production of methanol is expected to increase from currently approximately

100 to 500 Mt in 2050[7,8] and the demand for Li-ion batteries from 230 GW h in 2020 to 1.3 TW h in 2030.[9] This makes it all the more important not only to be able to control precipitation

Table 1. Phases Relevant for the Cu/Zn and Ni/Mn Systems in This Work and Their Solubility Products Available in the Literature

phase	molecular formula	system	K_{SP} (25°C)	$f(T)$?	year	ref(s)
–	$Mn_4(OH)_6SO_4$	Ni/Mn	$\approx 10^{-36}$	no	2022	29
–	$Ni(OH)_2$	Ni/Mn	7.94×10^{-17}	no	1997	18
			6.03×10^{-16}	no	2009	22
			1.07×10^{-17}	yes	2014	17
pyrochroite	$Mn(OH)_2$	Ni/Mn	2.00×10^{-13}	no	2009	17, 22
			1.58×10^{-13}	no	2004	39
			1.91×10^{-13}	no	1999	40
malachite	$Cu_2(OH)_2CO_3$	Cu/Zn	6.92×10^{-34}	no	2007	41
rosasite	$Cu_{1.16}Zn_{0.84}(OH)_2CO_3$	Cu/Zn	3.98×10^{-37}	no	1980	15
rosasite	$Cu_{1.4}Zn_{0.6}(OH)_2CO_3$	Cu/Zn	3.98×10^{-37a}	no	2017	42
aurichalcite	$Zn_{2.27}Cu_{2.73}(OH)_6(CO_3)_2$	Cu/Zn	7.94×10^{-91}	no	1980	15
hydrozincite	$Zn_5(OH)_6(CO_3)_2$	Cu/Zn	10^{-75b}	yes	2001	43
gerhardtite	$Cu_2(NO_3)(OH)_3$	Cu/Zn	1.82×10^{-33}	no	unknown	39
			1.78×10^{-33}	yes	unknown	44
			8.13×10^{-37}	no	2010	14
rouaite	$Cu_2(NO_3)(OH)_3$	Cu/Zn	1.91×10^{-36}	no	2010	14

^{a}Adopted from ref 2 for different stoichiometry. ^{b}Derived.

processes precisely but also to optimize them economically and in terms of product quality.

One approach for the control and optimization of these operations is the knowledge- and model-based process description by means of solid formation kinetics and/or the thermodynamic equilibrium. This always requires knowledge of the underlying solubility equilibria between the various solid phases and the liquid phase.[10] These substance-specific equilibria are quantified as temperature-dependent solubility products for sparingly soluble salts. In addition, the correct description of hydrochemistry and possible mixing phenomena are, in general, necessary for a knowledge-based process description.[11,12]

However, due to the very limited solubility of sparingly soluble salts in water of less than 1 g·L^{-1}, the determination of their solubility products requires particularly accurate and time-consuming measurements and complex analyses.[13] In general, a saturated solution is formed by adding a surplus of the solid phase in question to a solution with a defined ionic strength I at a defined temperature T. The suspension is then stirred for more than a week in order to ensure that the solubility equilibrium is achieved.[14] After filtration, ion concentrations in the saturated solution are quantified by elemental analysis[14,15] or by electrochemical means.[16] Then, using the stoichiometry of the salt, the concentrations are converted to the sought solubility product. The complex multistep methodology results, despite thorough work, in vastly deviating values, e.g., for $Ni(OH)_2$ where results between $K_{SP,Ni(OH)_2} = 1.07 \times 10^{-17}$[17] and $K_{SP,Ni(OH)_2} = 7.94 \times 10^{-17}$[18] are reported for 25 °C. Applying these different values to kinetic solid formation modeling results in supersaturations which differ by several orders of magnitude. This in turn results in nucleation rates and particle sizes that differ by several orders of magnitude.[10] Thus, careful evaluation of available data is required.

For other industrially significant substances, e.g., Cu/Zn-based catalyst precursors or Ni/Mn-based PCAM, which are both prepared by co-precipitation, solubility products are partially unavailable or sparse. One reason for this is the aforementioned complexity of K_{SP} measurements, which is why they are, in general, not carried out within the framework of

process modeling where the focus is on the prediction of particle sizes[19] or the composition.[20] Instead, authors rely on existing K_{SP} which are often only available for 25 °C and for mineral phases similar to the synthetic phases under consideration.[19−22] However, mineral and synthetic phases often differ in the following properties:

- Crystallographic properties: synthetic materials are formed much faster than their mineral counterpart which often results in smaller crystallites or distorted and amorphous solids as authors have shown, e.g., for the precipitation of the PCAM $Ni(OH)_2$ and $Mn(OH)_2$[3,23,24] or in the preparation of Cu/Zn-based catalyst precursors where, first, the amorphous phase georgeite $(Cu_2CO_3(OH)_2)$ is formed instead of the crystalline and better characterized phase malachite $(Cu_2CO_3(OH)_2)$.[25,26]

- Incorporation of foreign anions into the crystal lattices: if precipitation takes place at nonstoichiometric conditions, supersaturation can be depleted by the incorporation of alternative ions which are present in abundance from the educts, such as the incorporation of varying amounts of sulfate ions instead of hydroxide ions into the β-$Ni(OH)_2$ (theophrastite) and $Mn(OH)_2$ (pyrochroite) lattices, which affected the quality of the resulting batteries.[27−29]

- Substitution of lattice cations: if multiple cations with similar ionic radius and same electric charge are available, they can substitute one another in their respective solid phase to a variable degree, as is the case with the characterized mineral phases malachite $(Cu_2CO_3(OH)_2)$ and rosasite $(Cu_{1.46}Zn_{0.54}CO_3(OH)_2)$.[30] For the synthetic material, which is referred to as zincian malachite instead of rosasite, arbitrary Zn fractions between 0 and 28 mol % were obtained.[31]

Accordingly, the second reason for the lack of solubility products is that all these effects influence the solubility behavior of the solids; cf. Table 1. Vice versa, it is also only possible to describe these effects with a thermodynamic model if the corresponding phases with their individual solubility products are distinguished. However, the shortage of available data regarding, among others, the temperature influence for the Cu/

Zn-based catalyst precursor[32] or the variable amount of SO_4^{2-} ions from the educt salts incorporated into $Ni(OH)_2$ and $Mn(OH)_2$, currently makes this impossible for these two exemplary cases.

Hence, an easily accessible method to determine reliable solubility products for synthetic precipitate phases as a function of temperature and elemental composition is necessary for the modeling of these complex (co-)precipitation processes. Two recent studies suggest a simplified procedure to estimate K_{SP} of synthetic phases from titration studies based on the correlation between pH, ion speciation in the liquid phase, and the solid–liquid equilibrium. Cornu et al. performed titration studies where, depending on the reactants used, $Mn(OH)_2$ or $Mn_4(OH)_6SO_4$ was formed.[29] They showed that solubility products can be estimated from these titration curves, explaining previously unexplainable pH curves. However, they focused on the experimental results as a proof of concept and did not elaborate how exactly the K_{SP} values were calculated from pH and "the expected concentration (···)". Güldenpfennig et al. conducted similar titration studies with the model system $BaSO_4$ as the precipitant and were able to optimize their kinetic precipitation model by applying the thus determined $K_{SP,BaSO_4}$ in combination with similarly determined surface energies σ.[10] They described the hydrochemistry with the Davies approach which is, in general, limited to ionic strengths of approximately 0.5 mol·L^{-1}.[33,34]

Our goal is to develop further this approach into a standard method for the fast, yet reliable determination of solubility products of sparingly soluble salts as a function of temperature, elemental composition, and crystallinity, which can also be applied for more complex solid phases and as an alternative to the complex and time-consuming methods discussed above. For this purpose, we combine experimental titration studies with a thorough characterization of the solid phases by combining XRD, FT-IR, ICP-OES, and CHNS analysis on the one side and an automated fitting routine for K_{SP} based on our thermodynamic equilibrium model describing the hydrochemistry at industrially relevant ionic strengths above 0.5 mol·L^{-1} and the solid–liquid equilibrium on the other side.

2. THERMODYNAMIC DESCRIPTION OF PRECIPITATION

Thermodynamic data, such as the solubility product K_{SP}, ion association constants in the liquid phase (K_{IA}), or the stoichiometry limitations of solid solutions, e.g., how much Zn can be incorporated in the zincian malachite phase $([Cu,Zn]_2CO_3(OH)_2)$, are necessary for the determination of the solid formation kinetics during (co-)precipitation and the thermodynamic solid–liquid equilibria. In the following, we provide an overview of the thermodynamic fundamentals, available solubility data, and how they can be applied to describe precipitation processes.

2.1. State-Of-The-Art. The driving force for the formation of a given solid j by precipitation is phase-specific supersaturation S_j according to eq 1. It is described in terms of the actual activities of solid-forming ions a_i in the solution, the solubility product $K_{SP,j}(T)$ of the solid phase j, and the stoichiometric coefficients $\nu_{i,j}$ and $\nu_\pm$, which is the sum of all $\nu_{i,j}$.

$$S_j = \left(\frac{\prod a_{i,j}^{\nu_{i,j}}}{K_{SP,j}(T)} \right)^{1/\nu_\pm} \tag{1}$$

The solubility product $K_{SP,j}$ according to eq 2 describes the equilibrium between the solid-forming ions i in the liquid phase and each solid phase j and is a function of the individual activities of each ion i of the solid j at thermodynamic equilibrium $a_{i,j}^*$ and its stoichiometric coefficient $\nu_{i,j}$.

$$K_{SP,j} = \prod a_{i,j}^{*\nu_{i,j}} \tag{2}$$

The activity a_i of an ion i can be calculated from its molality b_i, the reference value $b^0 = 1 \text{ mol·kg}^{-1}$ solvent and its activity coefficient γ_i according to eq 3. Thus, nonideal ion interactions are considered.

$$a_i = \gamma_i \cdot \frac{b_i}{b^0} \tag{3}$$

According to eq 4, the amount of available solid-forming ions b_i, also referred to as free ions or dissociated ions, is further reduced by speciation reactions and the formation of complexes k where $\nu_{i,k}$ is the stoichiometric coefficient for the ion i in complex k. Additionally, b_i is further reduced by the formation of the solid phase.

$$b_i = b_{i,\text{total}} - \sum_k \nu_{i,k} \cdot b_k - \sum_j \nu_{i,j} \cdot b_j \tag{4}$$

The respective equilibrium is described with the ion association constant according to eq 5.

$$K_{IA,k} = \frac{a_k}{\prod a_{i,k}^{\nu_{i,k}}} \tag{5}$$

As stated previously, K_{SP} values are, in general, determined by elaborate equilibrium studies.[15,16] Similar approaches are established for the determination of K_{IA} in the liquid phase.[35] An overview of the available K_{SP} for the most relevant phases for the two substance systems considered here is given in Table 1. Values are often only available for 25 °C which prevents the modeling of temperature-dependent effects, especially since the precipitation in both examples is, in general, conducted at 50–70 °C.[3,36−38] Additionally, the variation of available K_{SP} for a single phase, e.g., $Ni(OH)_2$, can lead to significant differences in the kinetic descriptions.[10]

Not only due to the limited data available, but also due to open question concerning the solid formation in co-precipitation, e.g., when solid solutions are formed instead of individual single phases, various simplified approaches are used in the literature. Para et al. used eq 6 to estimate the mean supersaturation S of a multicomponent $[Ni_{0.8}Mn_{0.1}Co_{0.1}](OH)_2$ PCAM assuming that in all cases a solid solution, thus a completely homogeneous material at the nanoscale, is formed and that the composition of the solid phase matches that of the liquid phase.[19]

$$S = \sqrt[3]{\frac{(a_{Ni^{2+}})^{0.8}(a_{Mn^{2+}})^{0.1}(a_{Co^{2+}})^{0.1}(a_{OH^-})^2}{(K_{SP}^{Ni(OH)_2})^{0.8} \cdot (K_{SP}^{Mn(OH)_2})^{0.1} \cdot (K_{SP}^{Co(OH)_2})^{0.1}}} \tag{6}$$

However, additional sulfate-containing phases may have to be considered.[27−29] Furthermore, $Ni(OH)_2$ and $Mn(OH)_2$ show diverging precipitation kinetics resulting in nonhomogeneous metal distributions in some cases.[45] For this reason, ammonia solution is often added to induce the complex formation of Ni^{2+} ions and $NH_3^{(aq)}$ in the liquid and, thus, control the supersaturation of $Ni(OH)_2(s)$.[3,46] Therefore, describing precipitation with a single K_{SP} has its limitations. Furthermore, both the degree of SO_4^{2-} incorporation as well as the spatial

distribution of the individual metals greatly affect the resulting capacity and cycle stability of the final Li-ion batteries.[47,48] This shows how important it is to develop tools that allow for the modeling of these phenomena.

Several authors described the co-precipitation step[21,42,49] as well as the subsequent aging step[26,32] of the Cu/Zn system thermodynamically with the mineral data available which is limited to 25 °C, strictly crystalline phases and certain metallic composition of the solid solutions aurichalcite and rosasite, cf. Table 1. Despite the limited data, a good agreement between the calculated and experimentally determined solid masses and pH was achieved for the co-precipitation step.[49] Yet, no studies comparing measured and calculated particle sizes are known. Studies showed a significant influence of both the presence of rosasite after aging as well as the amount of Zn incorporated in zincian malachite $\tilde{x}_{Zn,metals,ZM}$ ($[Cu_{1-\tilde{x}_{Zn,metals,ZM}}Zn_{\tilde{x}_{Zn,metals,ZM}}]_2CO_3$-$(OH)_2$), cf. eq 26 later on, on the later catalyst performance.[50,51] Thus, in addition, a prediction of the phase composition in the solids after aging as well as $\tilde{x}_{Zn,metals,ZM}$ would be advantageous for the optimization of catalyst preparation. However, the temperature influence on the resulting solid-phase composition as well as the influence of metallic reactant ratios deviating from the stoichiometries of the aforementioned mineral phases cannot be reliably quantified using the solubility products of the related mineral phases.[32]

In summary, several, in parts successful, approaches to model the co-precipitation of Cu/Zn-based catalyst precursors and Ni/Mn-based PCAM exist. However, key characteristics of the co-precipitates, which are crucial for the later product qualities, such as the incorporation of SO_4^{2-} ions into the PCAM, the deviating precipitation kinetics of $Ni(OH)_2$ and $Mn(OH)_2$, or the complex-phase transitions, and solid solution behavior of the Cu/Zn-based precursors cannot be predicted reliably with the solubility data currently available.

2.2. Thermodynamic Modeling and Activity Coefficient Model. The elemental composition[1] and phase composition[52] of the co-precipitate, its total solid mass concentration in the suspension, the particle morphology[53] and size distributions[3] as well as the spatial homogeneity of the particles[47] are the key properties which determine the economic viability of the process and the resulting product qualities. The latter three are a result of the phase-specific solid formation kinetics. Additional to accurate solubility products $K_{SP,j}$, kinetic models require, among others, the surface energy σ_j for each solid phase j, for which reliable values in the literature are even more sparse.[10] Since our focus is on the determination of K_{SP} and the evaluation of the determined values, we confine ourselves to a thermodynamic equilibrium model, where σ_j is irrelevant, with the supersaturation S_j, the phase composition, and the solid mass concentrations as the relevant output sizes. For the same reason, mixing influences are also not considered here. Thus, in accordance with eqs 1–5, the accuracy of our calculations are exclusively a function of the speciation calculations, the activity coefficient model, and $K_{SP,j}$ itself.

The software PHREEQC (iphreeqc version 3.7.1)[54] is applied to calculate the thermodynamic state of equilibrium by solving the system of equations which results from the solid–liquid equilibria, speciations as well as mass and substance balance equations, cf. eqs 1–5. PHREEQC also calculates the activity of ions in the liquid phase by using appropriate activity coefficient models like the Pitzer or the SIT model, which are discussed below. For communication, import of the database and the input

variables, and output of the target parameters, Matlab (R2021a) is used. An ideally mixed isotherm system is assumed. By iteration, these calculations are repeated until all phases considered are saturated or undersaturated.

Input parameters of the thermodynamic equilibrium model are the total reactant molalities $b_{reactants,total}$, the water mass M_{H_2O}, the temperature T and, if an exchange between the gas phase and liquid phase is considered, the partial pressure of CO_2 p_{CO_2}. Furthermore, a fixed pH and degree of interaction with the gas phase can be chosen. The separate database contains all necessary substance data, in particular the speciation equilibria $[K_{IA,k}(T)]$, phase-specific solubility products $K_{SP,k}(T)$, and the stoichiometry of phases, as well as an activity coefficient model. Accordingly, the accuracy and completeness of the underlying databases regarding those equilibrium reactions determine the accuracy of the model calculations. Based on the number and validity of available data, the Pitzer approach is used for the Cu/Zn system (Pitzer.dat; iphreeqc version 3.7.1[54]) and the specific ion interaction theory (SIT) for the Ni/Mn system (ThermoChimie SIT v10a[17]) resulting in two separate databases. The accuracy of the speciation data and activity coefficient models applied were verified by Guse et al. for the Cu/Zn-based system.[32]
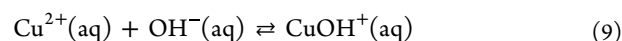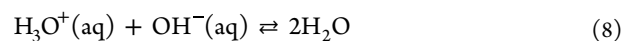
The temperature dependency is either specified by analytical expressions for $K_{SP,k}(T)$ and $K_{IA,k}(T)$ or given by the respective value at $T^0 = 298.15$ K and a standard reaction enthalpy $\Delta H_{R,k}^0$. $K_{SP,k}(T)$ and, accordingly, $K_{IA,k}(T)$ can then be calculated using the van't Hoff equation given in eq 7.
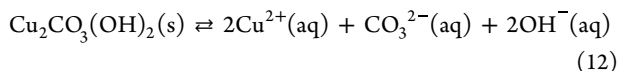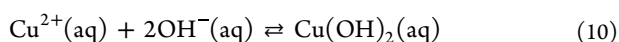
$$\ln\left(\frac{K_{SP,k}(T)}{K_{SP,k}(T^0)}\right) = \frac{\Delta H_R^0}{R}\left(\frac{1}{T^0} - \frac{1}{T}\right) \tag{7}$$

Further output variables apart from the supersaturation S_j are the molality $b_{S,j}$ for each solid phase j considered, the activities of each species i in the liquid phase a_i, and the pH. For the standard case, we assume that there is no interaction between the liquid and the atmosphere so that any CO_2 formed remains dissolved. We consider two different states:

- $t = t_{init}$: a hypothetical initial state after mixing of the reactant solutions is completed, but no solids were formed yet. We use this state to calculate initial supersaturation $S_{j,init}$, which we presume as the main driving forces for solid formation in co-precipitation.
- $t = t_{eq}$: the state of equilibrium where all considered solids phases are saturated or undersaturated. This state is applied to validate and determine $K_{SP,j}$ and to calculate the phase composition of the co-precipitate.

2.3. Model-Based Determination of Solubility Products from Titration Experiments. Based on the approaches described in the literature,[10,29] we want to determine pH as a function of the reactant ratio in titration experiments and use this data in combination with our thermodynamic equilibrium model in a fitting routine to determine solubility products of sparingly soluble salts unavailable in the literature. The key is the correlation between pH, speciation in the liquid phase, and the equilibrium between the liquid and solid phase which is illustrated below using the simplified example of $Cu_2CO_3(OH)_2$ (georgeite) in eqs 8–12.

$$H_3O^+(aq) + OH^-(aq) \rightleftarrows 2H_2O \tag{8}$$

$$Cu^{2+}(aq) + OH^-(aq) \rightleftarrows CuOH^+(aq) \tag{9}$$

$$Cu^{2+}(aq) + 2OH^-(aq) \rightleftharpoons Cu(OH)_2(aq) \qquad (10)$$

$$CO_3^{2-}(aq) + H_3O^+(aq) \rightleftharpoons HCO_3^-(aq) + H_2O \qquad (11)$$

$$Cu_2CO_3(OH)_2(s) \rightleftharpoons 2Cu^{2+}(aq) + CO_3^{2-}(aq) + 2OH^-(aq) \qquad (12)$$

pH is inversely correlated to the activity of H_3O^+ ions $a_{H_3O^+}$ and can be measured accurately over a broad range with standard lab equipment making it an ideal measurand. The experimental setup is described in Section 3.2. One reactant solution, here, $Na_2CO_3^{(aq)}$, is placed as the analyte. The other, here, $Cu(NO_3)_2^{(aq)}$, is then added dropwise as the titrant. Due to the autoprotolysis of water according to eq 8, H_3O^+ and OH^- ions are in equilibrium. Accordingly, one key prerequisite for the method introduced here is that at least one ion of the salt to be investigated [here $Cu_2CO_3(OH)_2$ in eq 12] forms a complex involving H_3O^+ or OH^- in the liquid phase. This is the case for Cu^{2+}, cf. eqs 9 and 10. Alternatively, the salt itself can contain H^+ or OH^- ions or complexes with foreign ions can be formed which in turn are at equilibrium with H_3O^+ or OH^-, e.g., CO_3^{2-} in eq 11. In any case, solid formation results in a shift in speciation which in turn influences the pH and the titration curve.

We ensure that solid formation is completed and in a (meta)stable state at each measurement point by waiting until pH is stable for 30 s. Thus, solid formation kinetics do not have to be considered and the thermodynamic equilibrium model allows a complete description of each individual process point of titration i if the speciation and solid−liquid equilibrium are correctly described in the model, cf. Section 2.2. Vice versa, a comparison of the pH values between the model and experiment allows an evaluation of the model quality. Figure 1 shows a comparison of a typical experimental titration curve for the precipitation of $Cu_2CO_3(OH)_2$ with two model calculations: one based on the application of literature data, cf. Table 1 and one using $K_{SP,j}$ values which were the result of our fitting routine.
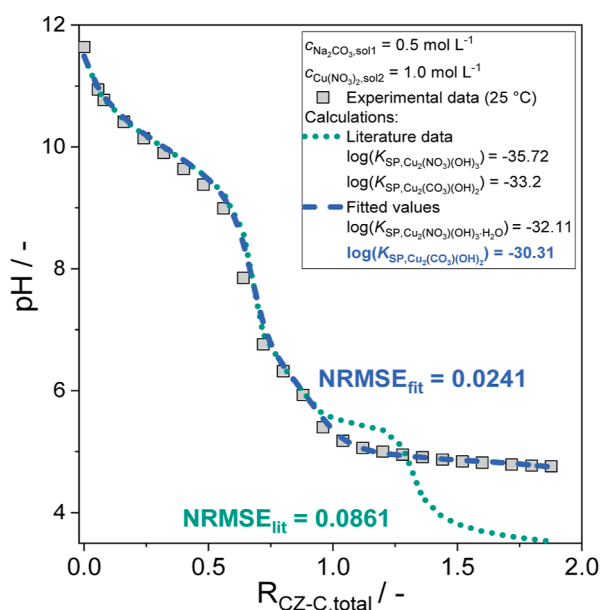

Figure 1. Comparison of the experimental titration curve of a $Cu_2CO_3(OH)_2$ precipitation with two model calculations.

Here, pH is plotted as a function of the total lattice ion ratio $R_{CZ-C,total}$ which is defined as follows

$$R_{CZ-C,total} = \frac{b_{Cu^{2+},total} + b_{Zn^{2+},total}}{b_{CO_3^{2-},total}} \qquad (13)$$

$R_{CZ-C,total} = 0$ indicates the start of the titration experiment with $Na_2CO_3^{(aq)}$ as the starting solution into which $Cu(NO_3)_2^{(aq)}$ is then added dropwise resulting in an increasing $R_{CZ-C,total}$. pH decreases slowly both in the experiment as well as in the model calculations mainly due to the formation of $Cu_x(CO_3)_y$ and $Cu_x(OH)_y$ complexes and the formation of the solid $Cu_2CO_3(OH)_2 \cdot H_2O$ (georgeite hydrate) as confirmed in the speciation calculation in Figure 2 as well as the XRD, FT-IR,
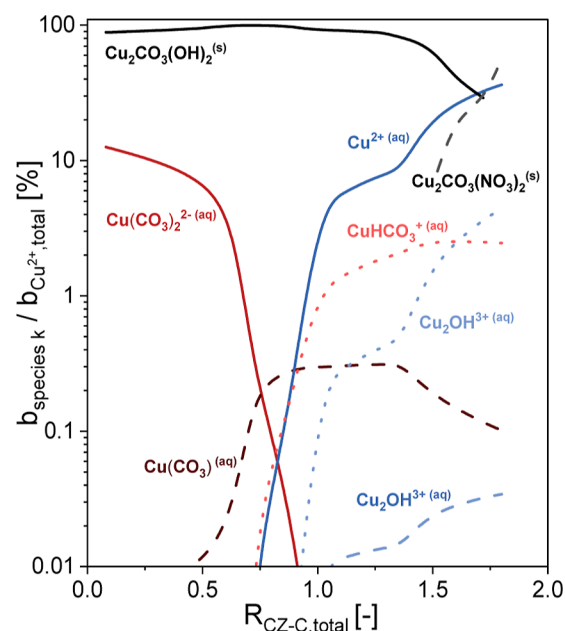
Figure 2. Calculated speciation and solid−liquid equilibrium for all Cu^{2+} species for the titration plotted in Figure 1.

and elemental analysis of the solids (cf. A.2 in Supporting Information). After a sharp decline at the stoichiometric ion ratio $R_{CZ-C,total} = 0.5$, a second plateau is present for $R_{CZ-C,total} \geq 1$ where, according to the model and solid analyses (cf. A.2 in Supporting Information), an increasing amount of the by-product $Cu_2(NO_3)_2(OH)_2$ (rouaite) of up to $x_{rou,solids} = 80.6$ wt % for $R_{CZ-C,total} = 1.6$ is formed.

In general, pH is influenced by three main factors: the speciation of Cu^{2+} according to Figure 2 and of all other ions present in the liquid phase, the validity of the activity coefficient model used, and the solubility products applied. Results in the literature[32] indicate that both the speciation calculations as well as the applied activity coefficient model are precise with deviations of less than 5% between measured and calculated pH in the parameter ranges considered. This is why we chose the Pitzer database for this study. Additionally, Figure 2 confirms that Cu^{2+} is mainly bound in the solid phases. The same also applies to the CO_3^{2-} and OH^- ions. This is due to the extremely low $K_{SP,j}$ values, cf. Table 1, which are integral for all sparingly soluble salts. For these reasons, the applied values for $K_{SP,j}$ are the main factor determining if the experimental pH pH_{exp} and the calculated pH pH_{calc} match. Still, the determined $K_{SP,j}$ is influenced by the speciation database and activity coefficient
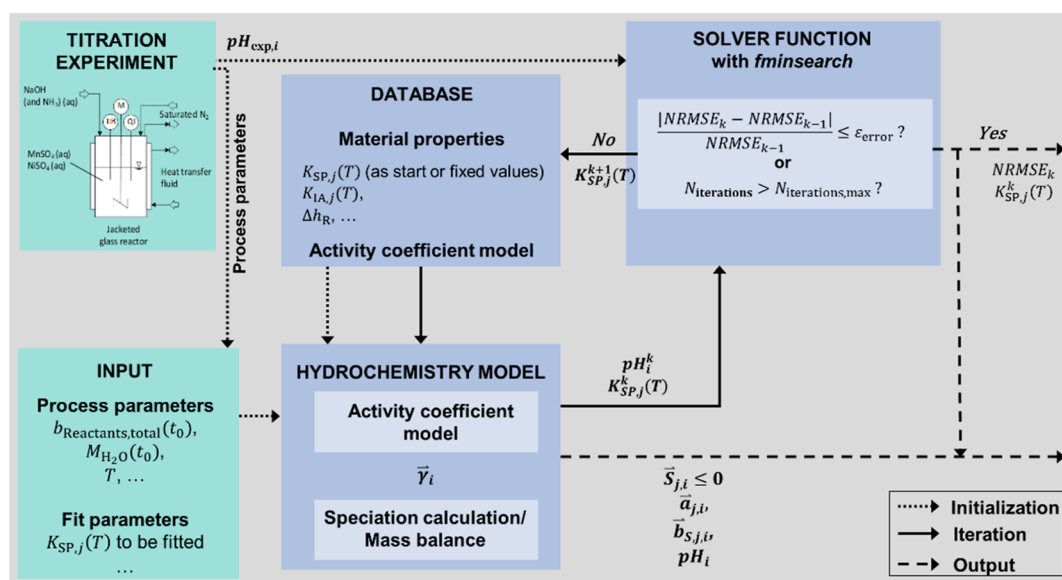
Figure 3. Schematic diagram of the fitting routine to determine $K_{SP,j}$ of sparingly soluble salts j by combining titration experiments and thermodynamic equilibrium calculations.

model used and, thus, should ideally be applied only in combination with the same database and activity coefficient model. However, for georgeite hydrate, no influence of the activity coefficient model and the database applied on the determined $K_{SP,georgeite}$ was apparent, cf. A.3 in Supporting Information.

The discrepancy between the experimental titration curve and the model calculations based on literature data which is evident in Figure 1 especially for $R_{CZ-C,total} \geq 1$ can be attributed to a possibly unsuitable $K_{SP,Cu_2CO_3(OH)_2}$ and/or $K_{SP,Cu_2(NO_3)_2(OH)_2}$. Hence, the fitting routine depicted in Figure 3 is applied to this exemplary case.

First, an experimental titration curve with as many sample points N as feasible is conducted, cf. Section 3.2. The applied process parameters are then used as inputs for a thermodynamic equilibrium calculation using the solubility products currently available. The normalized root mean squared error (NRMSE) is calculated according to eq 14 to quantify the difference between the measured and calculated pH curve. For each experimental sample point i with a corresponding $pH_{exp,i}$, a separate thermodynamic equilibrium calculation is conducted resulting in $pH_{calc,i}$. The arithmetic mean pH $\overline{pH}_{exp}$ results from eq 15.

$$NRMSE = \frac{\sqrt{\frac{\sum_{i=1}^{N}(pH_{calc,i} - pH_{exp,i})^2}{N}}}{\overline{pH}_{exp}} \qquad (14)$$

$$\overline{pH}_{exp} = \frac{\sum_{i=1}^{N} pH_{exp,i}}{N} \qquad (15)$$

Next, NRSME is minimized iteratively by varying, depending on the chosen input, one or more $K_{SP,j}$ until the target error is achieved or, due to the highly nonlinear correlations, a local minimum for NRMSE is found and further variation of $K_{SP,j}$ shows no improvement. For this purpose, the solver *fminsearch* in Matlab (R2021a) is used. Due to the strong non-linearity, the choice of the starting value for $K_{SP,j}$ is important. Besides NRMSE, an analysis of the solids formed during titration by XRD and elemental analysis is essential to validate the solid-

phase composition calculated by the model. Solid analysis is also required if the solid phases currently present in the model are not sufficient to describe the precipitation process and new solid phases have to be integrated into the model; see Section 4.1.1 concerning the incorporation of SO_4^{2-} into PCAM.

For the example titration, our fitting routine resulted in a much smaller error ($NRMSE_{fit} = 0.0241$) than to the use of literature data ($NRMSE_{fit} = 0.0731$) which is also evident in Figure 1. This way, to our knowledge, we were able to determine solubility data for synthetic amorphous $Cu_2CO_3(OH)_2 \cdot H_2O$ (georgeite hydrate) ($K_{SP,Cu_2CO_3(OH)_2} = 10^{-30.3\pm0.14}$) for the first time. The specified uncertainty results from the independent evaluation of the three titrations. The data can now be used instead of the solubility product for the naturally occurring mineral malachite ($K_{SP,Cu_2CO_3(OH)_2} = 10^{-33.2}$) for modeling the precipitation of the intermediate phase. These seemingly small differences for $K_{SP,Cu_2CO_3(OH)_2}$ result in supersaturations differing by a factor of up to 10 and differences of up to 50% for the precipitate mass for typical process conditions.[32]

Accordingly, our approach to determine $K_{SP,j}$ has proven to be suitable and is applied in Section 4 to, first, obtain missing $K_{SP,j}$ for the two substance systems. The applicability of the thus obtained data is then validated by modeling chosen co-precipitation processes.

3. EXPERIMENTAL METHODS

3.1. Materials. The purities of the key reactants given by the suppliers were verified by ICP-OES and CHNS analysis, cf. A.1 in Supporting Information.

3.2. Titration Studies. PCAM

For the titration experiments, one reactant solution, e.g., a $MnSO_4/NiSO_4$ (both ≥99% purity, Carl Roth GmbH) solution using deionized water (<50 $\mu S \cdot cm^{-1}$), was supplied in a temperature-controlled reactor (500 mL, ±1 K) while the other [e.g., a NaOH (≥98% purity, Carl Roth GmbH) solution] was slowly added via a buret. Thus, the reactions according to eqs 18 and 19 take place, and the resulting pH was measured (HI11310, Hanna Instruments). For all precipitations with manganese compounds, the deionized water was first degassed by boiling

and the experiment was conducted under a saturated nitrogen atmosphere to prevent oxidation of the Mn(II) species to e.g., Mn(III), Mn(IV), or Mn(VII) phases.[3] The pH electrode was calibrated daily (error below ± 0.02) with four reference solutions (pH buffer solutions 4.01; 7.00; 10.01; 13.00 $\pm$ 0.05, Carl Roth GmbH).

3.2.1. Cu/Zn-Based Catalyst. For the Cu/Zn system, the alkaline Na_2CO_3 ($\geq$99% purity, Carl Roth GmbH) solution was supplied in the reactor in order to prevent the formation of $CO_2(g)$ at small pH. Then, a solution of $Cu(NO_3)_2$ ($\geq$99% purity, Acros Organics) and/or $Zn(NO_3)_2$ ($\geq$99% purity, Alfa Aeser) was added for the formation of (zincian) malachite, cf. eq 12. A magnetic stirrer (250 or 500 rpm) was used for mixing.

The titration experiment ended when the equivalence point had been reached, and pH approached an asymptotic limit. For sampling, the titration was ended at defined volumes, and the suspension was filtered in its entirety to (a) guarantee a representative sampling and (b) to prevent the existence of not clearly defined reactant ratios and volumes after sampling. If possible, each titration was conducted thrice.

For cleaning, a 4% oxalic acid (oxalic acid dehydrate, $\geq$99% purity, Carl Roth GmbH) was used for the Ni/Mn system and a 2% HCl solution (from a 25% solution, Carl Roth GmbH) was used for the Cu/Zn system.

3.3. Application Studies. For the application studies for the Cu/Zn-based catalyst precursors, a micromixer setup is used which is described in detail elsewhere.[26] The mixer has two inlets with $d_i = 0.5$ mm which are arranged at an angle of 150°, cf. A.1 in the Supporting Information. Through these inlets the reactant solutions are supplied into the reaction chamber with a volume of 22 mm³ ensuring high and homogeneous energy dissipation rates and thus fast mixing where mixing influences on the solid formation are ruled out.[26] An adapted materials testing machine (Z010, Zwick/Roell GmbH&Co. KG) with two integrated syringes allows strictly defined volume flow rates up to 1500 mL·min⁻¹ (error < 1%) at high pressures ($p_{max} \approx 31$ bar). The reactant tanks, syringes, and the micromixer are temperature-controlled (RC6, Lauda with external Pt100; ± 1 K). pH was measured if relevant (HI11310, Hanna Instruments). The reactant solutions were prepared as described previously in Section 3.2. For some experiments, NaHCO₃ ($\geq$99% purity, Carl Roth GmbH) instead of Na₂CO₃ was used as the precipitant.

For the application studies regarding the Ni/Mn-based PCAM, a separate plant with two syringe pumps (Nexus 6000, Chemyx Inc.); two temperature-controlled reactant vessels ($V =$ 2000 mL, ± 1 K); a similar micromixer, cf. A.1 in Supporting Information; and a product vessel ($V = 1000$ mL) were used. Here, a saturated N₂ atmosphere was realized in each plant component to prevent oxidation of the Mn(II) reactants.

Each pump comprises four syringes (60 mL, BD Plastipak) to maximize the available volume for each measurement, e.g., to exclude start-up effects. The maximum total flow rate is 720 mL· min⁻¹ with an error of less than 1%. The total volume flow strongly correlates with energy dissipation rates and mixing times which, in turn, may influence the co-precipitation.[12,49] Thus, studies on the influence of mixing on the co-precipitate morphology and composition were conducted to determine an operating window of the plant where mixing effects on the solid formation are ruled out, cf. A.4 in Supporting Information. The reactant solutions were prepared as described previously in Section 3.2. The pH was measured if necessary (HI11310, Hanna Instruments). A 5% oxalic acid solution and deionized

water were used for in situ cleaning of the micromixer. The micromixer was regularly disassembled to check for depositions.

3.4. Solids Analysis. A combination of analysis techniques was applied to characterize the precipitated solids in order to verify if the assumed solid phases were formed. When XRD analysis confirmed the existence of solely amorphous phases, FT-IR measurements were applied supplementary.

3.4.1. Sample Preparation. All sample suspensions were filtered using a Büchner funnel with a diameter of 55 or 185 mm and glass fiber round filters ($\geq$0.6 μm, Macherey-Nagel) under vacuum (100 mbar). The filter cake was either washed by resuspending it in deionized water using a disperser at 3200 rpm (T 25 Ultra-Turrax with S 25 N−18 G, IKA) (Cu/Zn system) or by displacement washing (Ni/Mn system) where the wash water was supplied carefully on the top of the filter cake to prevent its damaging. Additionally, an overflow with saturated N₂ minimized oxidation.

Washing was completed when the conductivity of the filtrate fell below 50 μS·cm⁻¹ (Profiline LF 197, WTW) and, in the case of the Cu/Zn system, the nitrate concentration dropped below 10 mg·L⁻¹ (Nitrate test strips, VWR). The conductivity meter was calibrated with two reference solutions (conductivity standards 1413 $\pm$ 1 and 84 $\pm$ 1 μS/cm, Carl Roth GmbH). The filter cake was then dried at $\vartheta = 30$ °C and approximately $p <$ 10 mbar for at least 15 h. Afterward, the dried samples were ground in a mortar to a powder until no more lumps were visually detected. Both solid and liquid samples were stored in small airtight glass containers.

3.4.2. X-ray Diffraction and Rietveld Refinement. X-ray diffraction (XRD) is applied to determine the crystalline composition of the powdered samples. We used a Panalytical X'Pert Pro (Malvern Panalytical) with a monochromatic X-ray light source (Cu Kα radiation, 1.54 Å wavelength, with a Ni filter). The diffraction pattern was measured in the range of 5° < 2θ < 80° over a period of 120 min.

The XRD diffractograms were analyzed using Rietveld refinement and Profex 5.1. Section A.5 in the Supporting Information gives an overview of the references used for each system.

3.4.3. Elemental Analysis. We used two complementary methods to determine the elemental composition of the samples: (1) inductively coupled plasma optical emission spectrometry (ICP-OES) for the total mass fractions of metals and (2) flame atomic emission spectrophotometry (F-AES) to determine the total mass fractions of the light elements (C, H, N, S). For each method, the samples were ground after drying was completed.

For ICP-OES measurements, 50−100 mg of the samples were first digested by adding 6 mL of 65% HNO₃ (subboiled) and 2 mL of 30% HCl (p.A.). The mixture was heated to 250 °C using a microwave system (Multivace 5000, Anton Paar). The temperature was held for 45 min. Subsequently, the digests were diluted to a total volume of 50 mL with ultrapure water ($\leq$0.75 μS·cm⁻¹) and analyzed with an iCAP 7000 (Thermo Scientific). The ICP multielement standard IV (Carl Roth GmbH) was applied for calibration and to check the stability of the system. The ICP-OES reference solution VHG-MISA6-500 (VHG Laboratories) was used for quality assurance.

Quantitative CHNS analysis was conducted in a Vario Micro Cube (Elementar Analysensysteme GmbH) by combustion analysis coupled with thermal conductivity detection and repeated once. The oxygen mass fraction x_O was then calculated

from all other fractions measured, assuming that no further elements are present.

The mass fraction of nitrogen $x_{N,total}$ in the solid Cu/Zn-based samples determined by CHNS analysis was applied to calculate the mass fraction of phase rouaite $(Cu(NO_3)(OH)_3)$ $x_{rouaite,solids}$ according to eq 16 under the assumption that all N atoms are present as NO_3 in the rouaite lattice. Here, $x_{N,rouaite}$ is the stoichiometric mass fraction of N in the rouaite lattice.

$$x_{rouaite,solids} = \frac{x_{N,total}}{x_{N,rouaite}} \quad (16)$$

3.4.4. Fourier Transform Infrared Spectroscopy. We applied Fourier transform infrared spectroscopy (FT-IR) spectroscopy for the phase identification of X-ray amorphous samples. For this purpose, 1 mg of the sample was added to an agate mortar together with 400 mg of KBr (≥99.5% purity, VWR Chemicals). The mixture was ground for 1 min and pressed into a disc $(h_{KBr\,disc} = 1\,mm)$ with a hydraulic press (10 tons, 1 min). The spectra were recorded with an Agilent 660-IR. Each spectrum was the average of 64 scans using a spectral resolution of $2\,cm^{-1}$. Before each measurement, the chamber was purged for 5 min with N_2 to remove any CO_2 from the chamber.

3.4.5. Transmission Electron Microscopy and Energy-Dispersive X-ray Spectroscopy. Transmission electron microscopy (TEM) imaging was realized with an FEI Osiris ChemiStem (200 kV). Energy-dispersive X-ray spectroscopy (EDXS) using an equipped Bruker Quantax system (XFlash detector) was used to examine the spatially resolved elemental distribution of metals inside the particles, as well as the quantitative metal composition. The dried sample was suspended in water by means of an ultrasound bath and then spread on a TEM gold grid by using an ultrasonic fogger for both measurements.

4. RESULTS AND DISCUSSION

Our first main goal is to determine the $K_{SP,j}$ of industrially relevant sparingly soluble salts, which are unavailable in the literature but necessary for the thermodynamically based modeling of precipitation processes with our newly developed fitting approach. Second, we wanted to verify the applicability and validity of the thus determined $K_{SP,j}$ in separate application studies. We conducted these studies for the two substance systems in Sections 4.1 and 4.2 to show the general applicability of our approach.

4.1. Ni/Mn-Based Precursors for Cathode Active Material. The focus of the titration studies with the Ni/Mn system is on the evaluation and possibly extension of available solubility data as a prerequisite for the thermodynamically based description of the co-precipitation of PCAM by applying our newly developed fitting routine. Since the main solids are $Mn(OH)_2$ and $Ni(OH)_2$, the prerequisite for applying our approach, that pH is influenced by solid formation, is met. We concentrate on the following three key questions:

- Can the fitting approach based on experimental titration studies and thermodynamic equilibrium calculations be applied to determine $K_{SP,j}$ for salts relevant as PCAM?
- Can the incorporation of sulfate into the solids and the temperature dependency be described with a thermodynamic equilibrium model?
- Is the approach suggested by Para et al., to consider the co-precipitation product as a single phase,[19] valid or is it necessary to consider multiple single-metal phases?

The total lattice ion ratio $R_{NM-O,total}$ is defined according to eq 17 and applied to plot titration curves independent of reactant concentrations and volumes. $R_{NM-O,total} = 0.5$ is equal to a stoichiometric precipitation of $Ni(OH)_2(s)$ and $Mn(OH)_2(s)$, respectively.

$$R_{NM\text{-}O,total} = \frac{b_{Mn^{2+},total} + b_{Ni^{2+},total}}{b_{OH^-,total}} \quad (17)$$

First, the single-metal solids $Mn(OH)_2$ and $Ni(OH)_2$, cf. eqs 18 and 19, as relevant PCAM are precipitated individually in titration studies.

$$Mn(OH)_2 \rightarrow Mn^{2+} + 2OH^- \quad (18)$$

$$Ni(OH)_2 \rightarrow Ni^{2+} + 2OH^- \quad (19)$$
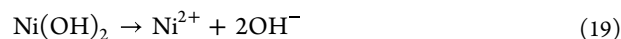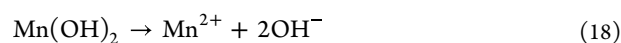
*4.1.1. Solubility Product of Mn(OH)2.* A titration curve for the formation of $Mn(OH)_2$ is depicted in Figure 4. Here,
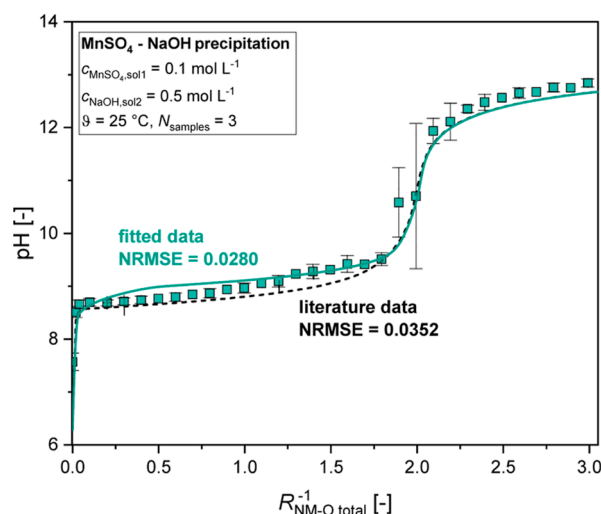
Figure 4. Comparison of the experimental titration curve of $Mn(OH)_2$ precipitation from $MnSO_4^{(aq)}$ with thermodynamic equilibrium model calculations based on available literature data and fitted data, respectively.

experimental data are compared to both a thermodynamic model based on literature data, cf. Table 1, as well as a model calculation with fitted data. The metal salt solution was used as the analyte. Thus, pH is plotted as a function of $R_{NM-O,total}^{-1}$ with $R_{NM-O,total}^{-1} = 0$ marking the start of the titration. Adding one drop of NaOH solution instantly results in pH > 8. Subsequently, due to the formation of $Mn(OH)_2(s)$ according to the speciation calculation in Figure 5, only a small pH increase is evident in both the experimental and model data up to the stoichiometric lattice ion ratio $R_{NM-O,total}^{-1} = 2$ where all Mn^{2+} ions present in the liquid are depleted. A further addition of OH^- ions results in a sudden OH^- surplus in the liquid and thus an abruptly increasing pH with the pH of the NaOH solution itself as the upper limit.

Due to the partial oxidation of samples taken at pH > 10, mainly to Mn_3O_4, during filtration and washing, the results of XRD and elemental analysis are inconclusive and not given here, cf. A.6 in Supporting Information. Both model variants using literature data $[\log(K_{SP,Mn(OH)_2,lit}) = -12.70]^{17}$ and a fitted solubility product for $Mn(OH)_2(s)$ $[\log(K_{SP,Mn(OH)_2,fit}) = -12.06 \pm 0.22]$, respectively, show a similar trend and depict
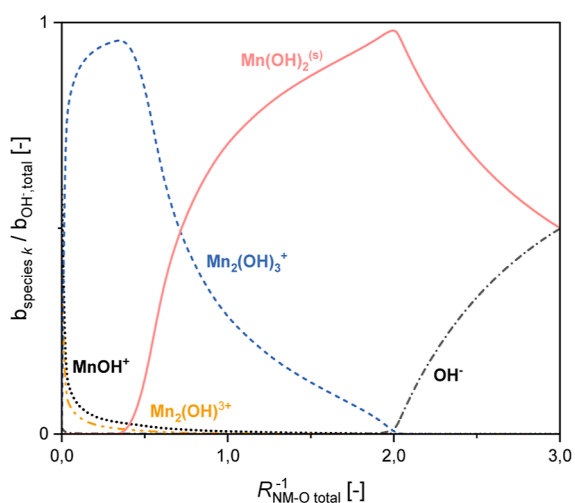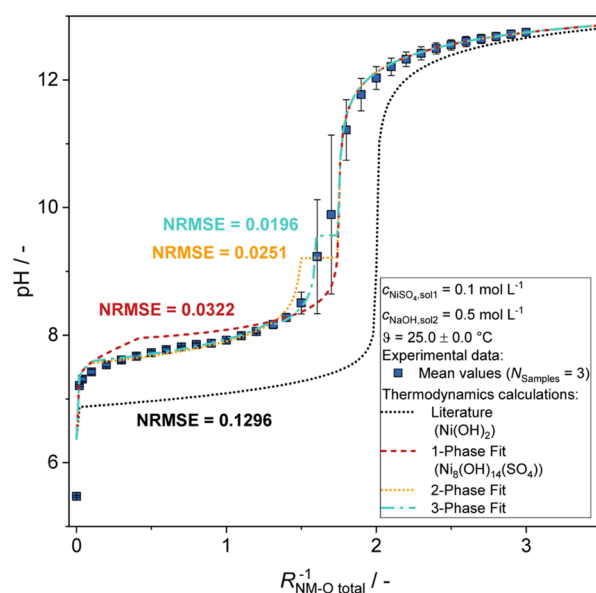
Figure 5. Calculated speciation and solid−liquid equilibrium for all OH⁻ species for the titration plotted in Figure 4 applying the fitted data.

Figure 6. Comparison of different modeling approaches concerning the incorporation of SO_4^{2-} into $Ni(OH)_2(s)$ to describe the experimental titration curve.

the experimental titration curve adequately ($NRMSE_{fit} \approx NRMSE_{lit} \ll 0.10$). The deviation of both K_{SP} may result from deviations in the speciation database or the activity coefficient model applied, cf. A.3 in Supporting Information. The specified uncertainty of the newly determined $K_{SP,Mn(OH)_2,fit}$ results from the evaluation of four independent titrations. In a similar titration conducted by Cornu et al., SO_4^{2-} ions were incorporated into the crystal lattice of $Mn(OH)_2(s)$.[29] This was not the case here; cf. Figures 11 and 12 which are discussed later on. A possible explanation is that the $Mn(SO_4)_2$ solution was higher concentrated in the study by Cornu et al. Thus, at a defined pH, the ratio between available SO_4^{2-} and OH⁻ ions is higher which may favor the incorporation of sulfate into $Mn(OH)_2(s)$. In summary, both the literature value for the mineral phase pyrochroite and the fitted data can be applied for modeling the PCAM synthesis.

Additionally, the procedure was repeated for $T = 60\ °C$, cf. A.6 in Supporting Information, to determine the temperature dependency of $K_{SP,Mn(OH)_2}$, which is unavailable in the literature. Thus, $\Delta H^0_{R,Mn(OH)_2} = -0.54\ kJ·mol^{-1}$ was calculated using eq 7 with $\log(K_{SP,Mn(OH)_2}(60\ °C)) = -12.07$ which is much smaller than the value for $Ni(OH)_2$ available in the literature: $\Delta H^0_{R,Ni(OH)_2} = -84.39\ kJ·mol^{-1}$[17] and might explain why the precipitation of $Ni(OH)_2$ dominates at elevated temperatures in a co-precipitation of both phases.[45]

4.1.2. Solubility Products of $Ni(OH)_2$ and Nickel Hydroxyl Sulfates as Possible Byproducts. The same procedure is repeated for the other main precipitate, $Ni(OH)_2$, as shown in Figure 6. In general, an experimental titration curve similar to that for $Mn(OH)_2$ is apparent. However, the sudden increase in pH, which indicates that all available Ni^{2+} ions are depleted, already occurs at $R^{-1}_{NM-O,total} = 1.75$. Thus, a clear deviation is evident for the model calculation using literature data where, as expected, the increase occurs at $R^{-1}_{NM-O,total} = 2$, the stoichiometric ion ratio for $Ni(OH)_2$. Rietveld refinement confirms β-$Ni(OH)_2$ (theophrastite) as the most probable phase but shows high uncertainties and small fractions of α-$Ni(OH)_2$ (jamborite), cf. Table 2 and Section A.6 in Supporting Information. These uncertainties most probably result from the small crystallite sizes, cf. Figure S.7 in Supporting Information, and the
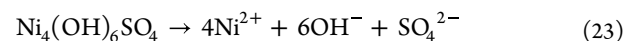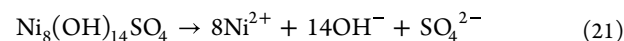
correlated peak broadening. An alternative explanation is that the precipitate is mostly or partly X-ray amorphous.

Furthermore, the elemental analysis data in Table 2 show that large amounts of sulfur ($x_S \geq 3.6\%$) are incorporated into the precipitate for $R^{-1}_{NM-O,total} < 2$, most probably as SO_4^{2-} ions. A significant drop in x_S is evident for $R^{-1}_{NM-O,total} \geq 2$ when there is a stoichiometric excess of OH⁻ ions with respect to $Ni(OH)_2$. Assuming that all available Ni^{2+}, OH⁻, and SO_4^{2-} ions form a common solid phase at $R^{-1}_{NM-O,total} = 1.75$, where the increase in pH occurs experimentally, $Ni_8(OH)_{14}SO_4$ results quantitatively from the molar ratio of the three ions as the theoretical solid phase, cf. eqs 20 and 21.

$$\text{For } R^{-1}_{NM-O,total} = 1.75: \frac{1}{8}b_{Ni^{2+},tot} = \frac{1}{14}b_{OH^-,tot} = b_{SO_4^{2-},tot} \tag{20}$$

$$Ni_8(OH)_{14}SO_4 \rightarrow 8Ni^{2+} + 14OH^- + SO_4^{2-} \tag{21}$$

$$Ni_5(OH)_8SO_4 \rightarrow 5Ni^{2+} + 8OH^- + SO_4^{2-} \tag{22}$$

$$Ni_4(OH)_6SO_4 \rightarrow 4Ni^{2+} + 6OH^- + SO_4^{2-} \tag{23}$$

Here, $x_S = 4.0\%$ is to be expected which matches well with the experimental x_S in Table 2. Our hypothesis is that due to a lack of OH⁻ ions, SO_4^{2-} ions are incorporated into a theophrastite (β-$Ni(OH)_2$)-like lattice instead. Similar phases with ratios of hydroxide to sulfate ions of 6 to 10 were reported for Cu and Al ($Cu_4(SO_4)(OH)_6·2H_2O$, $Al_4(SO_4)(OH)_{10}·5H_2O$)[55] as well as, more recently, for Mn ($Mn_5(OH)_8SO_4$,[56] $Mn_9(OH)_{14}(SO_4)_2·H_2O$,[57] $Mn_4(OH)_6SO_4$[29]).

Compared to the model variant with literature data (NRMSE = 0.1296), a much better agreement between the model and measurement is achieved when applying the model variant based on $Ni_8(OH)_{14}SO_4$ (NRMSE = 0.0322). When applying models with multiple $Ni_x(OH)_y(SO_4)_z$ phases, in order to address the variable x_S as a function of $R^{-1}_{NM-O,total}$, the deviation can be further reduced to NRMSE = 0.0196. The corresponding speciation and solid−liquid equilibria are included in Supporting Information, cf. Figure S.19. However, the implementation

Table 2. Influence of $R^{-1}_{\text{NM-O,total}}$ on pH, the Solid Phase Composition Analyzed by XRD, and the Elemental Composition Determined by ICP-OES

			$x_i/(\text{g·g}^{-1})$ in %			
$R^{-1}_{\text{NM-O,total}}$	pH	$x_{j,\text{solids,XRD}}/(\text{g·g}^{-1})$	Ni	O	H	S
0.8	7.72	$x_{\beta\text{-Ni(OH)}_2,\text{solids}} = 0.79 \pm 0.65$[a]	50.4	44.2	2.7	3.6
1.5	8.24	$x_{\beta\text{-Ni(OH)}_2,\text{solids}} = 0.85 \pm 0.24$[a]	49.6	45.2	2.6	4.2
2.2	12.27	$x_{\beta\text{-Ni(OH)}_2,\text{solids}} = 0.82 \pm 0.86$[a]	49.0	45.8	2.8	1.9
expected for β-Ni(OH)$_2$		$x_{\beta\text{-Ni(OH)}_2,\text{solids}} = 1.0$	63.3	34.5	2.2	0
expected for Ni$_8$(OH)$_{14}$SO$_4$		$x_{\text{Ni(OH)}_2,\text{solids}} \approx 1.0$	58.4	35.8	1.8	4.0

[a]Indicates a mostly X-ray amorphous sample.

Table 3. Overview of the Newly Determined Solubility Products and Comparison with Data Available in the Literature for Relevant Ni^{2+} Phases[a]

|	25 °C	60 °C	$\Delta H^0_R/\text{kJ·mol}^{-1}$
$\log(K_{\text{SP,Ni(OH)}_2}/\text{mol}^3\,\text{L}^{-3})$	n.a. ($-16.1;$[18] $-17.0;$[17] -17.5[58])	-14.69 ($-15.81;$[17] -13.45[59])	76.60 (95.4[17])
$\log(K_{\text{SP,Ni}_8\text{(OH)}_{14}\text{SO}_4}/\text{mol}^{23}\,\text{L}^{-23})$	-104.2 ± 0.29 (n.a.)	n.a.	n.a.
$\log(K_{\text{SP,Ni}_5\text{(OH)}_8\text{SO}_4}/\text{mol}^{14}\,\text{L}^{-14})$	-62.5 ± 0.13 (n.a.)	n.a.	n.a.
$\log(K_{\text{SP,Ni}_4\text{(OH)}_6\text{SO}_4}/\text{mol}^{11}\,\text{L}^{-11})$	-48.0 ± 0.05 (n.a.)	n.a.	n.a.

[a]n.a.: not available.

of multiple phases, e.g., in a kinetic model would result in a higher model complexity and increased computing times. Ideally, a solid phase with a variable S fraction would be used. Nevertheless, the newly proposed Ni$_8$(OH)$_{14}$SO$_4$ phase and its determined solubility product are suitable means for describing the Ni(OH)$_2$ precipitation. All determined solubility products are summarized in Table 3 along with temperature-dependent data.

In summary, the conducted titration studies and elemental analyses for the precipitation of Ni(OH)$_2$ suggested that SO$_4^{2-}$ ions are incorporated into the crystal lattice, especially for $R^{-1}_{\text{NM-O,total}} < 2$. Thus, we identified possible Ni$_x$(OH)$_y$(SO$_4$)$_z$ phases and determined the $K_{\text{SP},j}$ for these to enable the modeling of SO$_4^{2-}$ incorporation in PCAM.

4.1.3. Application of the Newly Determined Solubility Products for Modeling the Co-precipitation of Ni(OH)$_2$ and Mn(OH)$_2$. A titration with the equimolar co-precipitation of Ni(OH)$_2$ and Mn(OH)$_2$ is depicted in Figure 7 in order to evaluate the applicability of the determined solubility products. Three model variants are compared with the experimental data: a calculation using literature data for the solubility products of Ni(OH)$_2$ and Mn(OH)$_2$, a variant with multiple Ni$_x$(OH)$_y$(SO$_4$)$_z$ phases, cf. eqs 21–23, and the fitted $K_{\text{SP},j}$ from Table 3; and last, a variant where a common Ni–Mn phase is implemented according to Para et al. and eq 6.[19]

It is evident from Figure 7 that the titration curve behaves similarly to a superposition of the single-phase titrations, cf. Figures 4 and 6, with a small increase in pH for small lattice ion ratios $R^{-1}_{\text{NM-O,total}}$ up to $R^{-1}_{\text{NM-O,total}} = 1$. Here, a change in the slope is apparent. The speciation of OH$^-$ in the liquid and solid phase as a function of $R^{-1}_{\text{NM-O,total}}$ in Figure 8 indicates that the changed slope might be due to the changed composition of the precipitate: from pure Ni(OH)$_2$ to a mixture of both hydroxides. This assumption is confirmed by the elemental analysis data summarized in Table 4. For $R^{-1}_{\text{NM-O,total}} < 2$, the solid is mostly composed of Ni with only small but increasing fractions of Mn. For $R^{-1}_{\text{NM-O,total}} > 2$, OH$^-$ ions are present superstoichiometrically and an equimolar amount of Ni and Mn is present in the solids as expected from the reactant concentrations. Rietveld refinement
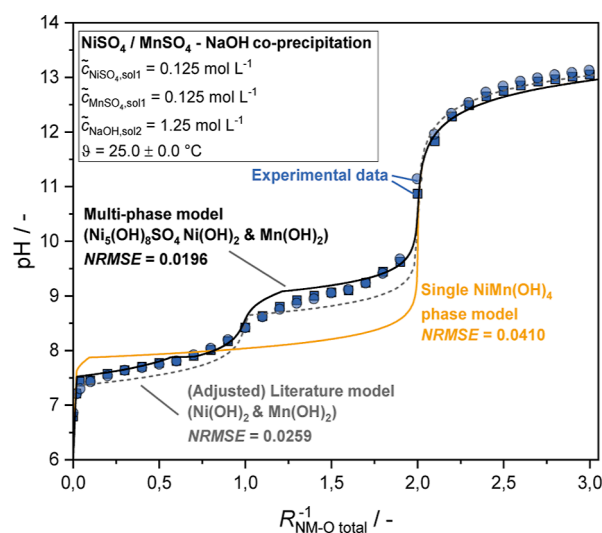
Figure 7. Comparison of different modeling approaches for the co-precipitation of Mn(OH)$_2$(s) and Ni(OH)$_2$(s).

of the XRD diffractograms further verify that the relevant solids phases are indeed Ni(OH)$_2$ and Mn(OH)$_2$, cf. A.6 in the Supporting Information and Table 4. Yet, the quantitative XRD analysis must be considered critically because of the strong peak broadening and thus resulting uncertainties.

For these reasons, the model approach with a single mixed Ni/Mn phase is unsuitable to describe the co-precipitation of Ni(OH)$_2$ and Mn(OH)$_2$ for $R^{-1}_{\text{NM-O,total}} < 2$. Integrating Ni$_5(OH)_8SO_4$ as an additional phase slightly increases the model accuracy (NRMSE$_{\text{fitted}} >$ NRMSE$_{\text{lit}}$). The more important advantage, however, is that the incorporation of SO$_4^{2-}$ ions can be modeled correctly for $R^{-1}_{\text{NM-O,total}} < 2$ by implementing Ni$_5$(OH)$_8$SO$_4$.

Finally, we want to evaluate the accuracy of the newly determined $K_{\text{SP},j}$ in the modeling of a scalable PCAM synthesis, which is not influenced by mixing, by using the micromixer setup described in Section 3.3. Based on the state-of-the-art in Section 2.1, we identified the lattice ion ratio $R_{\text{NM-O,total}}$, which is strongly
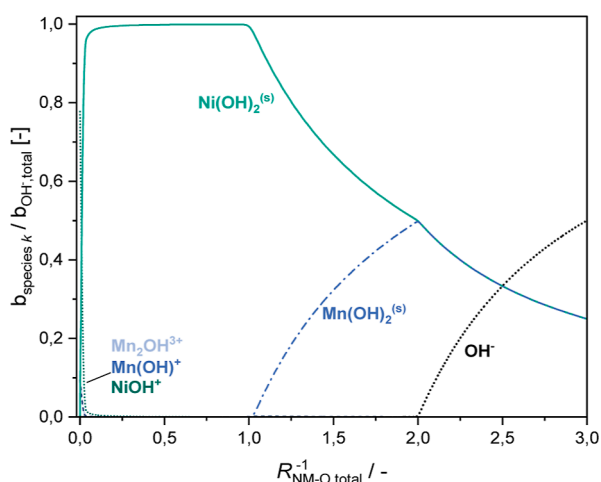
Figure 8. Calculated speciation and solid−liquid equilibrium for all OH⁻ species for the titration plotted in Figure 7 and the SIT model variant with Ni(OH)₂(s) and Mn(OH)₂(s).

Figure 9. Influence of $\tilde{c}_{\mathrm{OH}^-,\mathrm{feed2}}$ on the molar Ni fraction relative to the total metal amount $\tilde{x}_{\mathrm{Ni,metals}}$.

correlated to the pH, as the most important process parameter to determine the composition of Ni/Mn-based co-precipitates. We describe the composition by means of two quantities: the Ni fraction of the total metal amount $\tilde{x}_{\mathrm{Ni,metals}}$ as defined in eq 24 and the molar amount of S incorporated into the lattice in relation to the total metal amount in the solid sample $R_{\mathrm{S-NM}}$ according to eq 25
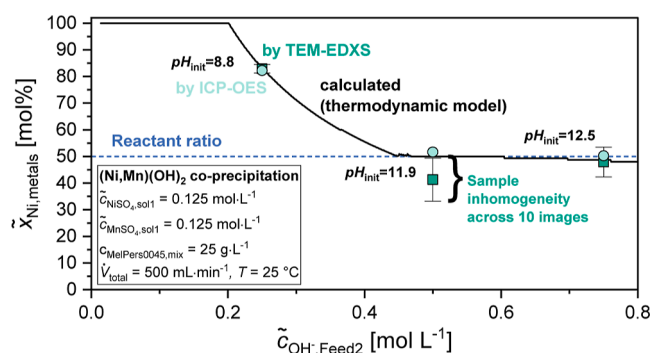
$$\tilde{x}_{\mathrm{Ni,metals}} = \frac{n_{\mathrm{Ni}}}{n_{\mathrm{Ni}} + n_{\mathrm{Mn}}} = \frac{\tilde{x}_{\mathrm{Ni,solids}}}{\tilde{x}_{\mathrm{Ni,solids}} + \tilde{x}_{\mathrm{Mn,solids}}} \quad (24)$$

$$R_{\mathrm{S-NM}} = \frac{\tilde{x}_{\mathrm{S,solids}}}{\tilde{x}_{\mathrm{Ni,solids}} + \tilde{x}_{\mathrm{Mn,solids}}} \quad (25)$$

The impact of $R_{\mathrm{NM-O,total}}$ on $\tilde{x}_{\mathrm{Ni,metals}}$ is investigated as shown in Figure 9 by varying $\tilde{c}_{\mathrm{OH}^-,\mathrm{feed2}}$ for $\tilde{c}_{\mathrm{metals,feed1}}$ = const.

Similarly to the co-titration of Ni(OH)₂ and Mn(OH)₂, an enrichment of Ni is evident for understoichiometric conditions ($\tilde{c}_{\mathrm{OH}^-,\mathrm{feed2}} < 0.5$ mol·L⁻¹, $R_{\mathrm{NM-O,total}} > 2$) both in the samples investigated by ICP-OES and TEM-EDXS as well as the model results. For increasing $\tilde{c}_{\mathrm{OH}^-,\mathrm{feed2}}$, the Ni fraction decreases until $\tilde{x}_{\mathrm{Ni,metals}} \approx 0.5$ is reached for $\tilde{c}_{\mathrm{OH}^-,\mathrm{feed2}} = 0.5$ mol·L⁻¹ which corresponds to the metal composition in the reactant solution. No deviations between the metal composition as predicted by the thermodynamic equilibrium model and the experimental data are evident.

The corresponding TEM-EDXS images in Figure 10 reveal inhomogeneous particles for pH$_{\mathrm{init}}$ = 11.9 and pH$_{\mathrm{init}}$ = 12.5, where areas of Ni and Mn enrichment are evident. This confirms

the need for the inclusion of separate Ni(OH)₂ and Mn(OH)₂ phases in the modeling independent from pH.

The TEM-EDXS images were also analyzed quantitatively regarding the molar fraction of S; cf. Figure 11. They visually confirm our assumption from the titration studies that for the process parameters considered, only Ni(OH)₂ tends to incorporate SO₄²⁻ ions. For this reason, the relative sulfur fraction $R_{\mathrm{S-NM}}$ is plotted as a function of $\tilde{x}_{\mathrm{Ni,metals}}$ as shown in Figure 12 for three total lattice ion ratios $R_{\mathrm{NM-O,total}}$ in order to (a) determine the main factors responsible for the SO₄²⁻ incorporation and (b) to evaluate if the enhanced model can predict the amount of incorporated SO₄²⁻. $R_{\mathrm{S-NM}}$ and $\tilde{x}_{\mathrm{Ni,metals}}$ were determined by both TEM-EDXS and ICP-OES.

In general, it is evident that higher $\tilde{x}_{\mathrm{Ni,metals}}$ result in higher $R_{\mathrm{S-NM}}$. Conducting the co-precipitation with at least the stoichiometric amount of OH⁻ ions ($R_{\mathrm{NM-O,total}} \leq 0.5$) decreases the amount of SO₄²⁻ incorporated into the solids. Both trends confirm the results from the titration experiments. By comparing the experimental data with the calculations, it is apparent that these general tendencies as well as the quantitative amount of incorporated sulfate ions for $R_{\mathrm{NM-O,total}} = 0.5$ and $R_{\mathrm{NM-O,total}} = 0.3$ can be predicted reliably. However, due to the nature of the model, the strong scattering of $R_{\mathrm{S-NM}}$ determined by TEM-EDXS for $R_{\mathrm{NM-O,total}} = 1.0$ cannot be reproduced. Still, the fraction of S in the total sample determined by ICP-OES is predicted correctly.

In summary, the application studies confirm that the thermodynamic equilibrium model based on the newly determined $K_{\mathrm{SP},j}$ can quantitatively describe the sulfate incorporation into the PCAM as well as the total Ni/Mn ratio as a function of pH and the reactant composition. Especially for $R_{\mathrm{NM-O,total}}^{-1} < 2$, where Ni(OH)₂ precipitates predominantly and SO₄²⁻ ions are incorporated at a large scale, the assumption of a common Ni/Mn mix phase is not recommended and Ni$_x$(OH)$_y$(SO₄)$_z$ phases should be implemented in the

Table 4. Influence of $R_{\mathrm{NM-O,total}}^{-1}$ on pH, the Solid Phase Composition Analyzed by XRD and the Elemental Composition Determined by ICP-OES

$R_{\mathrm{NM-O,total}}^{-1}$	pH	$x_{j,\mathrm{solids,XRD}}$	$x_i/(\mathrm{g\cdot g^{-1}})$ in %			$\tilde{x}_{\mathrm{Mn,metals}}$
[-]	[-]	[-]	Ni	Mn	S	[%]
0.4	7.68	n.a.[a]	24.3	1.9	2.1	7.8
1.3	8.73	$x_{\mathrm{Mn(OH)_2,solids}}$ = 0.48; $x_{\mathrm{Ni(OH)_2,solids}}$ = 0.52	22.6	9.0	2.3	29.9
2.8	12.97	$x_{\mathrm{Mn(OH)_2,solids}}$ = 0.46; $x_{\mathrm{Ni(OH)_2,solids}}$ = 0.54	19.3	17.9	0.5	49.7

[a]n.a. is not available.
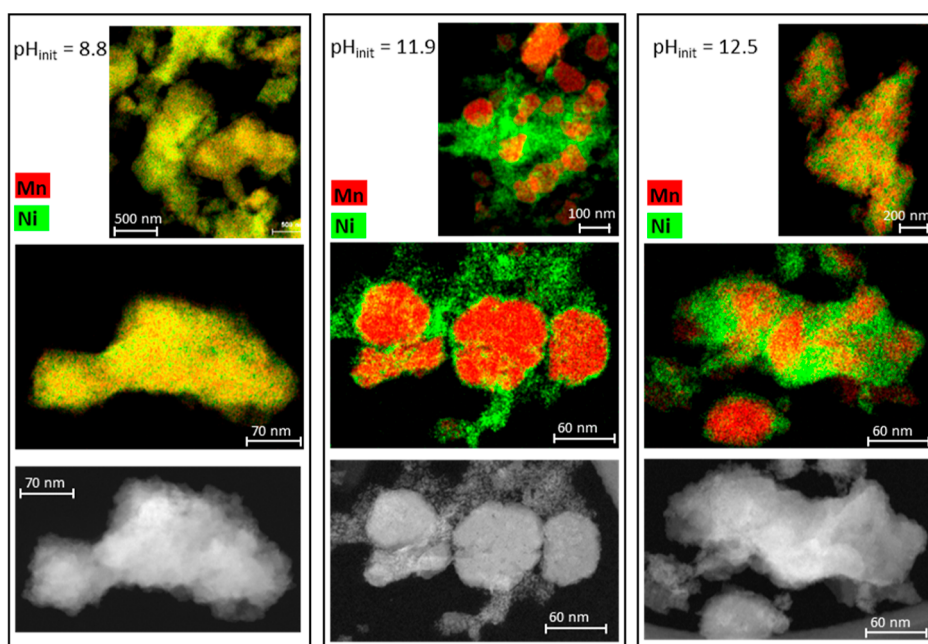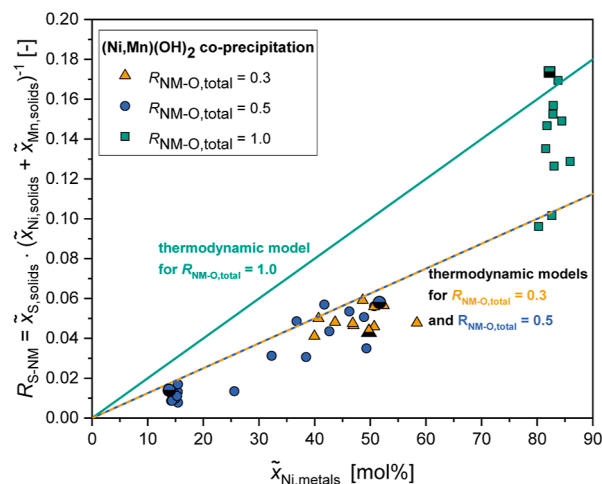
Figure 10. TEM-EDXS images of co-precipitated $Ni(OH)_2/Mn(OH)_2$ particles prepared at different initial pH values with Mn highlighted in red and Ni in green.
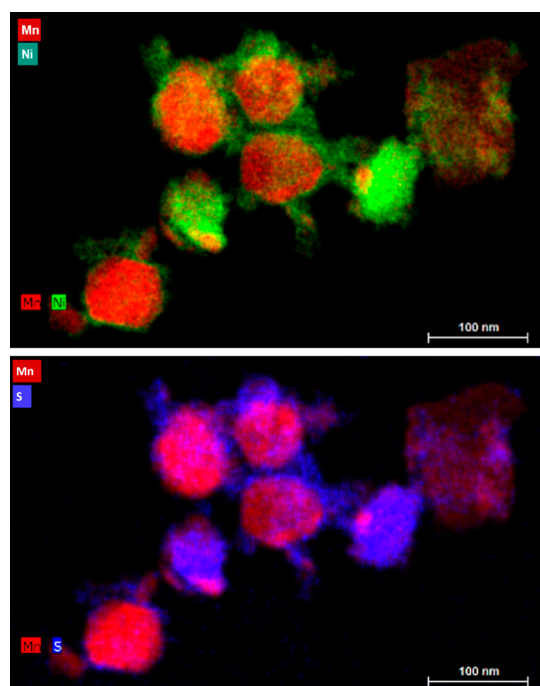
Figure 11. TEM-EDXS images of co-precipitated $Ni(OH)_2/Mn(OH)_2$ for $\tilde{x}_{Ni,metals} \approx 0.5$ and $R_{NM-O,total} = 0.3$ showing the spatial distribution of Ni and Mn (top image) and Mn and S (bottom image), respectively.
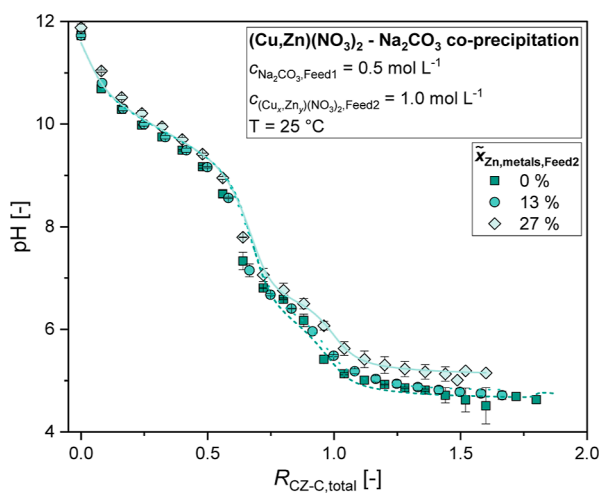

Figure 12. Influence of the Ni fraction in the total metal amount $\tilde{x}_{Ni,metals}$ on the molar S amount relative to the total metal amount R_{S-NM} for different $R_{NM-O,total}$ determined by TEM-EDXS [$\square,\bigcirc,\triangle$] and ICP-OES [$\blacksquare,\bullet,\blacktriangle$].

thermodynamic model. Thus, our newly developed approach to determining $K_{SP,j}$ from titration curves is suitable for the development and improvement of thermodynamically based precipitation models.

4.2. Cu/Zn-Based Catalyst Precursors. The most relevant Cu/Zn phases in the preparation of Cu/Zn-based catalysts are the precipitate phase (zincian) georgeite ($[Cu,Zn]_2CO_3(OH)_2$),the corresponding aged precursor phase (zincian) malachite ($[Cu,Zn]_2CO_3(OH)_2$) and aurichal-

cite ($[Zn,Cu]_5(CO_3)_2(OH)_6$). Since solubility data for these phases, especially for $T > 25 \,°C$ and Cu/Zn ratios deviating from the boundary compositions are mostly unavailable, cf. Table 1, our focus is on the determination of their $K_{SP,j}$ as a function of temperature and the Zn fraction $\tilde{x}_{Zn,metals}$ according to eq 26.

$$\tilde{x}_{Zn,metals} = \frac{n_{Zn}}{n_{Zn} + n_{Cu}} \tag{26}$$

Additionally, the influence of the process time t_{age} on $K_{SP,Cu_{1.46}Zn_{0.54}CO_3(OH)_2}$ will be investigated in order to evaluate if the solubility data for the amorphous phase directly after co-precipitation (zincian georgeite) and the data for the crystalline phase after aging (zincian malachite) are interchangeable, as assumed in the literature so far.[49]

4.2.1. Influence of the Zn Fraction and the Aging Time on the Solubility of (Cu,Zn)₂CO₃(OH)₂. First, the influence of the molar Zn fraction $\tilde{x}_{Zn,metals}$, as defined in eq 26, on the solubility product of zincian georgeite (ZG) $K_{SP,ZG}$ is investigated with the titration experiments as shown in Figure 13. Each titration was

Figure 13. Influence of the Zn fraction in (zincian) georgeite on the titration curve.

conducted three times. The pH curve is plotted as a function of the total lattice ion ratio $R_{CZ-Z,total}$ for three different Zn fractions in the titrant solution $\tilde{x}_{Zn,metals,feed2}$.

For $R_{CZ-C,total} = 0$, the pure Na_2CO_3 solution is present. Adding the $Cu(NO_3)_2/Zn(NO_3)_2$ solution results in an almost linear pH decrease and immediate solid formation, which is attributed to (zincian) georgeite according to the phase composition as shown in Figure S.20 in the Supporting Information based on model calculations and XRD and CHNS analysis. For $R_{CZ-Z,total} = 0.8$, the XRD diffractograms of all samples indicate an amorphous nature of the respective sample, cf. the Supporting Information. There are two possible reasons for this: for one, the crystallites are so small that peak broadening dominates and individual peaks are not distinguishable anymore. However, samples prepared under similar conditions but with $R_{CZ-C,total} = 1.6$ or $\tilde{x}_{Zn,metals} > 0.5$ do show peaks, cf. the Supporting Information. Furthermore, doubling the dwell time while maintaining the number of steps during XRD analysis does not influence the resulting diffractogram. Both indicate that peak broadening due to small crystallites is not the reason for the amorphous diffractogram. The more probable reason for this is that the solid itself has an amorphous structure. Of all possible phases, only (zincian) georgeite is known to be amorphous regardless of the particle size.[60] Complementary FT-IR analysis confirms (zincian) georgeite as the sole phase; cf. Section A.2 in the Supporting Information.

From $R_{CZ-C,total} \approx 0.6$ on, the pH decline increases for all $\tilde{x}_{Zn,metals,feed2}$ until a nearly constant pH arises for $R_{CZ-C,total} > 1.1$ which can be attributed to additional formation of rouaite $(Cu_2(NO_3)(OH)_3)$ as a byproduct, cf. Figure S.20 in Supporting Information. An evaluation of the titration curves with our fitting routine for $R_{CZ-Z,total} \leq 0.8$, where no rouaite is formed, results in a correlation between the solubility product and the Zn fraction in the solid sample $\tilde{x}_{Zn,metals,ICP}$ which are summarized in Table 5.

Table 5. Influence of the Zn Fraction in $[Cu_{1-\tilde{x}_{Zn,metals,ZG}}, Zn_{\tilde{x}_{Zn,metals,ZG}}]_2CO_3(OH)_2$ (Zincian Georgeite) on the Determined Solubility Product[a]

$\tilde{x}_{Zn,metals,feed2}$	0%	13%	16%	27%
$\tilde{x}_{Zn,metals,ICP}(R_{CZ-C,total} = 0.8)$	0.15%	11.32%	n.a.	24.29%
$\tilde{x}_{Zn,metals,ICP}(R_{CZ-C,total} = 1.6)$	0.08%	9.96%	n.a.	13.67%
$\tilde{x}_{Zn,metals,ZG}$	0.15%	11.32%	16%	24.29%
$\log(K_{SP,fit}/mol^5 \cdot L^{-5})$	−30.66	−30.59	−30.32	−29.99
$\log(K_{SP,lit}/mol^5 \cdot L^{-5})$	−33.2[41]	n.a.	n.a.	−36.4[15]

[a]n.a.: not available.

Compared to the solubility data for the crystalline phases available in the literature, significantly smaller values for $K_{SP,ZG}$ were determined here for each $\tilde{x}_{Zn,metals,ZG}$, cf. eq 26 and Section 2.1. Furthermore, the trend in $K_{SP,ZG}$ as a $f(\tilde{x}_{Zn,metals,ZG})$ is reversed in comparison to the two data points available in the literature, cf. Table 1: the determined $K_{SP,ZG}$ increases with increasing $\tilde{x}_{Zn,metals,ZG}$. Additionally, the actual Zn fraction of the solid $\tilde{x}_{Zn,metals,ZG}$ is compared to the feed composition. For $R_{CZ-C,total} = 0.8$, $\tilde{x}_{Zn,metals,feed2} \approx \tilde{x}_{Zn,metals,ZG}$ is valid meaning that Zn is completely precipitated and incorporated into the zincian georgeite lattice. The lowered Zn fraction for $R_{CZ-C,total} = 1.6$ is attributed to the increasingly predominant formation of rouaite instead of zincian georgeite, cf. Figure S.20 in the Supporting Information.

Next, we evaluate if the solubility of the initial co-precipitate (zincian georgeite) and the aged material (zincian malachite) differ. We believe that due to the metastable nature of the initial amorphous co-precipitate,[61] separate data is necessary to adequately describe both intermediates and the transformation between both. Thus, $Cu_{1.46}Zn_{0.54}CO_3(OH)_2$ titrations were performed for three different aging times t_{age} in Figure 14. For the fast titration to investigate the initial co-precipitation, a maximum of $t_{age} = 30$ s passed between two measuring points resulting in a total titration time of less than 10 min. For the other two variants, aging times of $t_{age} = 2$ h, respectively $t_{age} \geq 5$ h, were realized in between each measurement point in order to
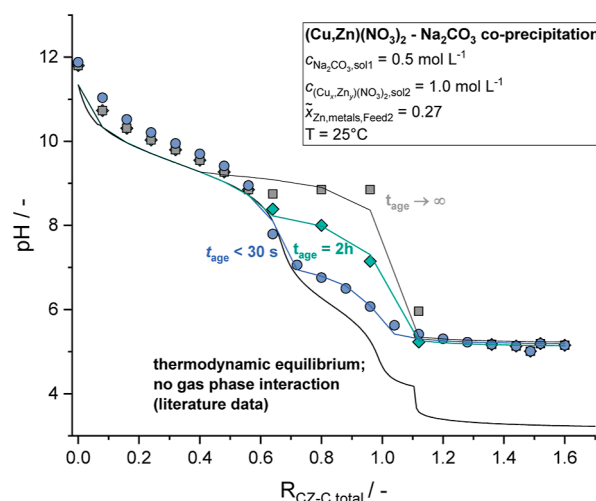
Figure 14. Influence of aging time on the titration curve of a $Cu_{1.46}Zn_{0.54}CO_3(OH)_2$ (zincian georgeite/malachite with $x_{Zn,ZM} = 0.27$) precipitation considering formation of $CO_2(g)$ compared to a thermodynamic model calculation with literature data and no $CO_2(g)$ formation.

**Table 6. Influence of the Aging Time t_{age} on the Determined Solubility Products of $Cu_{1.46}Zn_{0.54}CO_3(OH)_2$ (Zincian Georgeite/Malachite with $\tilde{x}_{Zn,metals,ZM} = 0.27$) and the Composition of the Solids Determined by ICP-OES and CHNS Analysis**

		$x_i(R_{CZ\text{-}C,total} = 0.8)/(g \cdot g^{-1})$ in %							
t_{age}	$\log(K_{SP,fit}(25\,°C)/mol^5\,L^{-5})$	Cu	Zn	Na	C	H	O[a]	N	$\tilde{x}_{Zn,metals,ZM}$ /mol·mol^{-1}
≤30 s	−32.97	37.27	14.25	0.25	5.5	1.5	41.0	0.22	0.267
2 h	−34.78	44.95	16.53	0	4.7	1.1	32.6	0.1	0.263
→∞ (>5 h)	−35.28	40.86	14.76	0	4.9	1.4	37.5	0.2	0.260
expectation zincian georgeite hydrate $(Cu_{1.46}Zn_{0.54}CO_3(OH)_2 \cdot H_2O)$	n.a.	38.64	14.70	0	5.0	1.7	40.0	0	0.27
expectation zincian malachite $(Cu_{1.46}Zn_{0.54}CO_3(OH)_2)$	$(-36.4^{15,42})$	41.77	15.90	0	5.4	0.9	36.0	0	0.27

[a]Value based on mass balance.

form an aged co-precipitate. XRD and FT-IR analyses confirm that amorphous zincian georgeite is formed for $t_{age} = 30$ s while crystalline zincian malachite is formed for $t_{age} \geq 2$ h, cf. A.7 in the Supporting Information.

It is evident from Figure 14 that the three respective titration curves differ significantly in the range $0.5 \leq R_{CZ\text{-}C,total} \leq 1.1$. A thermodynamic model based on literature data and the assumption that no $CO_2(g)$ is formed is inadequate to describe any of the three curves. Thus, the fit routine was applied in order to consider a possible influence of the aging time on $K_{SP,Cu_{1.46}Zn_{0.54}CO_3(OH)_2}$ and on the equilibrium between dissolved and outgassed CO_2 according to eq 27.

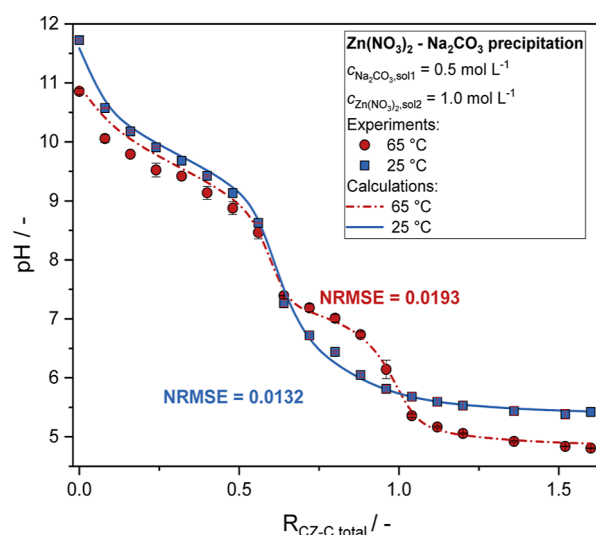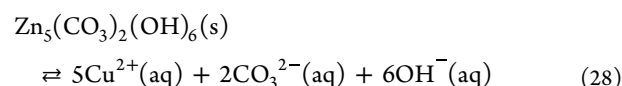$$CO_3^{2-} + 2H_3O^+ \rightarrow 3H_2O + CO_2(g) \tag{27}$$
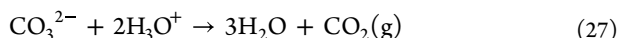
This results in the data summarized in Table 6. The thus updated models are able to reproduce the respective titration curves in Figure 14. The molar amount of solids and $CO_2(g)$ formed per kg of H_2O (b_i) is plotted in Figure S.21 in the Supporting Information and suggests that the $CO_2(g)$ formation is the main attributor for the aforementioned differences in the titration curves.

The main finding from Table 6 is that the solubility of $Cu_{1.46}Zn_{0.54}CO_3(OH)_2$ decreases significantly with increasing aging times. This is consistent with the typical phase transformation during aging where zincian georgeite transforms into zincian malachite.[32] The elemental analysis data in Table 6 confirms that the targeted Zn fraction $\tilde{x}_{Zn,metals,ZM} = 0.27$ and elemental composition of zincian malachite is realized for $t_{age} = 2$ h. For $t_{age} = 30$ s, the data suggests the formation of a hydrate $(Cu_{1.46}Zn_{0.54}CO_3(OH)_2(H_2O))$. The lower solubility product for $t_{age} = 30$ s compared to the values in Table 5 are the result of applying $K_{SP,rouaite} = 1.91 \times 10^{-36}$ as a boundary condition to reduce the degrees of freedom in the calculation.[14] This emphasizes the importance of careful selection of compatible solubility products and activity coefficient parameters in a model.

In summary, we successfully applied the newly developed fitting tool to determine $K_{SP,ZG}(\tilde{x}_{Zn,metals,ZG})$. Furthermore, we verified that the solubility products for the amorphous metastable phase zincian gerogeite and its crystalline, aged counterpart zincian malachite differ significantly. In both cases, $K_{SP,j}$ were previously unavailable in the literature.

4.2.2. Temperature-Dependent Solubility Products of Copper and Zinc Salts. Due to the lack of data in the literature, the temperature dependency of $K_{SP,j}$ for the main solids phases (zincian) georgeite, (zincian) malachite, aurichalcite, and hydrozincite was investigated by conducting titration studies at multiple temperatures. Figure 15 exemplarily shows the

titration curve and fitted model curves for hydrozincite, cf. eq 28, for 25 and 65 °C.

$$\begin{aligned} Zn_5(CO_3)_2(OH)_6(s) \\ \rightleftharpoons 5Cu^{2+}(aq) + 2CO_3^{2-}(aq) + 6OH^-(aq) \end{aligned} \tag{28}$$

Figure 15. Influence of temperature on the titration curve of $Zn_5(CO_3)_2(OH)_6$ (hydrozincite).

In general, the two curves show a similar trend as a function of the total reactant ratio: a decline that can be attributed to the addition of acidic metal nitrate solution and simultaneous formation of $Zn_5(CO_3)_2(OH)_6$ as confirmed by XRD analysis and model calculations, cf. Figure S.22 in the Supporting Information. Yet, in the range $0.6 \leq R_{CZ\text{-}C,total} \leq 1.1$ a distinct deviation between the curves is evident. The limited solubility of CO_2 at elevated temperatures is a possible reason for this phenomenon. Thus, we implemented eq 27 into our thermodynamic model.

Figure S.22 in the Supporting Information verifies that the calculated amount of $CO_2(g)$ indeed increases with temperature. Taking the $CO_2(g)$ formation into account allows the determination of the temperature-dependent solubility products for hydrozincite and analogue for the other five phases. The thus determined $K_{SP,j}(T)$ for these solids are summarized in Table 7. Using eq 7 a mean standard reaction enthalpy ΔH_R was calculated from the three temperature-specific solubility products.

Table 7. Influence of Temperature on the Determined Solubility Products of Zincian Georgeite (ZG) ($Cu_{1.46}Zn_{0.54}CO_3(OH)_2\cdot$ H_2O), Georgeite ($Cu_2CO_3(OH)_2\cdot H_2O$), Zincian Malachite (ZM) ($Cu_{1.46}Zn_{0.54}CO_3(OH)_2$), Malachite ($Cu_2CO_3(OH)_2$), Aurichalcite ($Zn_{2.9}Cu_{2.1}(CO_3)_2(OH)_6$) and Hydrozincite ($Zn_5(CO_3)_2(OH)_6$) Compared to the Data Available in the Literature

| T/°C	25 °C	45 °C	65 °C	ΔH_R^0/kJ·mol^{-1}
$\log(K_{SP,ZG}(T)/mol^6\cdot L^{-6})$	−32.97	−33.63	−34.22	−103.7 ± 31.2
$\log(K_{SP,georgeite}(T)/mol^6\cdot L^{-6})$	−33.77	−32.30	−32.5	60.2 ± 41.1
$\log(K_{SP,ZM}(T)/mol^5\cdot L^{-5})$	−34.78 (−36.4[15,42])	−35.44	−36.03	−60.2 ± 15.5
$\log(K_{SP,malachite}(T)/mol^5\cdot L^{-5})$	−35.02 (−33.2[41])		−33.99	49.5
$\log(K_{SP,aurichalcite}(T)/mol^{13}\cdot L^{-13})$	−76.16 (−90.1[15])	−79.05	−82.19	−292.4 ± 20.9
$\log(K_{SP,hydrozincite}(T)/mol^{13}\cdot L^{-13})$	−72.73 (−75.27[43])	−73.29 (−74.32)	−73.62 (−73.48)	−42.6 ± 5.7 (86.5)

Applying $K_{SP,rouaite} = 1.82 \times 10^{-33}$[39] instead of $K_{SP,rouaite} = 1.91 \times 10^{-36}$[14] as a boundary condition resulted in a significantly different $\log(K_{SP,aurichalcite}(65\ °C)/mol^{13}\ L^{-13}) = -89.05$ which also affected the applied model calculations discussed in Section 4.2.3. Thus, for aurichalcite, an alternative analytical expression for the temperature dependency was deduced additionally, cf. Supporting Information.

In summary, we were able to determine $K_{SP,j}(T)$ for the synthetic solid phases (zincian) georgeite, (zincian) malachite, aurichalcite, and hydrozincite by applying the newly developed fitting routine.

4.2.3. Modeling the Precursor Co-precipitation and Aging Using the Determined Solubility Products. In the preparation of the Cu/Zn based catalyst, zincian georgeite as an amorphous intermediate is first formed by the initial co-precipitation.[21,42,62] The particle properties of this intermediate can influence the subsequent process as well as the final product properties[36] which is why a reliable model is essential. Thus, the impact of the newly determined solubility product for zincian georgeite on the model quality compared to the use of literature data for rosasite is evaluated in Figures 16 and 17 where the solid mass of the co-precipitate as a function of the reactant concentration and the pH of the suspension are displayed.

As to be expected for a maximum yield, the concentration of zincian georgeite in the suspension $c_{zG,susp}$ increases linearly with the concentration of Cu and Zn in the feed solution $\tilde{c}_{reactants,feed2}$ both in the experiment and model calculations. For low concentrations, both models result in similar values. However, due to the smaller solubility assumed in the literature ($K_{SP,ZG} \approx$
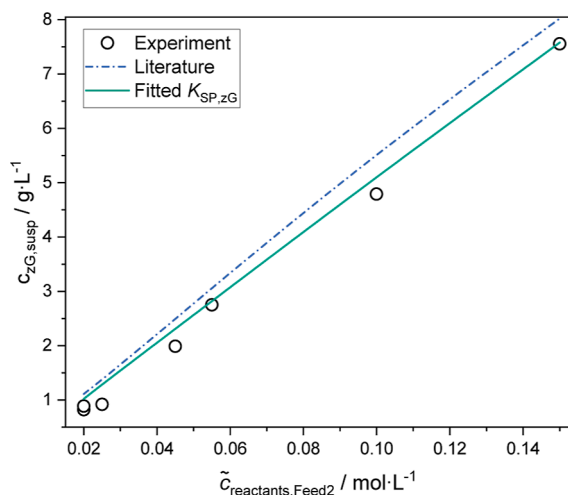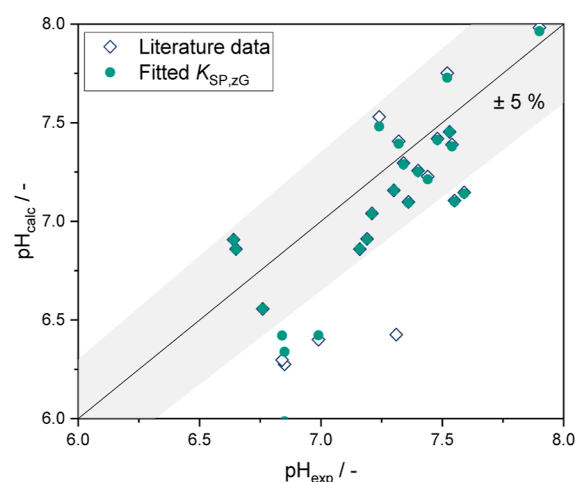
Figure 17. Comparison of the calculated and experimentally determined pH under variation of reactant concentrations at 55 °C.

$K_{SP,rosasite} = 3.98 \times 10^{-37}$), $c_{zG,susp}$ is increasingly overestimated for larger feed concentrations compared to the experimental data. Meanwhile, the model matches the experimental data for high $\tilde{c}_{reactants,feed2}$ if the adjusted solubility product $[K_{SP,ZG}(55\ °C) = 2.34 \times 10^{-35}]$ is applied.

For the pH variation in Figure 17 $R_{CZ-C,total}$ was varied by adjusting the reactant concentrations and, in some cases, HNO_3 and NaOH were added to adjust pH. The pH range was chosen so that zincian georgeite remains the only product. Both model variations behave similarly and mostly show deviations of less than 5% compared to the experimental data. The remaining uncertainties are a result of the activity coefficient model, as well as the speciation equilibria applied. Yet, in some cases where large amounts of HNO_3 were added ($\tilde{c}_{HNO_3,feed2} > 0.1\ mol\cdot L^{-1}$), the deviation of the literature model is increased compared to the model variant with the adjusted $K_{SP,ZG}$.

During the subsequent aging step the intermediate then transforms, depending on the exact process parameters, into zincian malachite, aurichalcite or byproducts such as rouaite which affects the homogeneity and specific surface area of the resulting catalyst.[26,32] In Figure 18 the solid phase composition after aging is plotted as a function of the temperature.

The experimental phase composition was determined by a Rietveld refinement of the dried material as described elsewhere.[32] It indicates that for a ratio of $n_{Cu,total} = 2n_{Zn,total}$ zincian malachite is formed exclusively up to $T = 60$ °C. For higher temperatures, the mass fraction of aurichalcite increases up to $x_{aurichalcite} \approx 26$ wt %. Since temperature dependent solubility products are not available for all phases in the literature, cf. Table 1, this effect cannot be described by applying the data from the literature. In contrast, by applying the

Figure 16. Comparison of the calculated and experimentally determined solid mass concentration of zincian georgeite as a function of the initial supersaturation S at 55 °C.
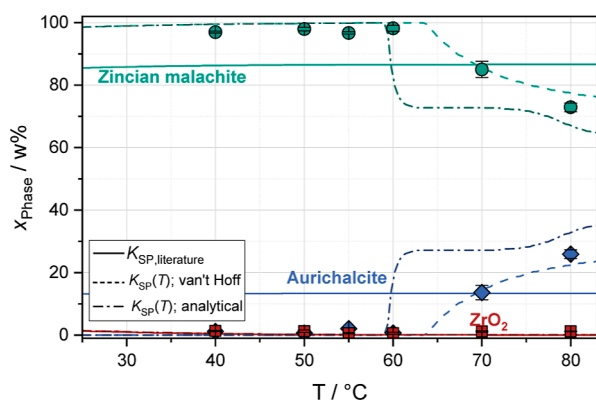
Figure 18. Comparison of the calculated and experimentally determined phase composition after aging for a Cu/Zn/Zr ratio of $n_{Cu,tot} = 2n_{Zn,total} = 6n_{Zr,total}$ as a function of the temperature. Data from ref 32.

solubility products determined by the titration studies, the formation of aurichalcite for $T > 60$ °C is correctly predicted regardless of which temperature dependency was applied for $K_{SP,aurichalcite}$, cf. Table 7.

Besides the temperature, the reactant ratio of Cu and Zn is known to determine the phase composition after aging.[36] Thus, its influence is plotted in Figure 19 for both experimental and
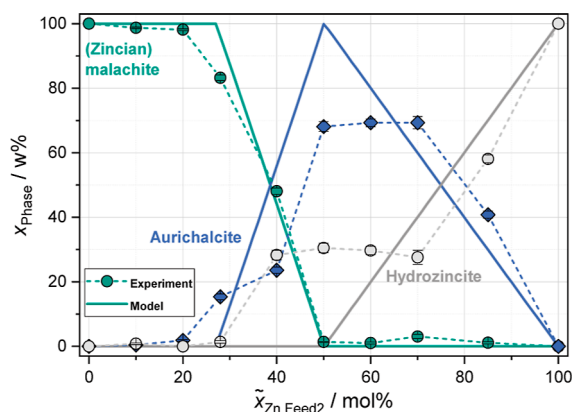
Figure 19. Solid phase composition as a function of the molar Zn fraction in the feed for $T = 65$ °C. Data from ref 32.

model data. Here, the analytical expression for $K_{SP,aurichalcite}$ was applied since $x_{aurichalcite}(65 \, °C)$ is underestimated when applying the van't Hoff equation. In general, the phase composition of the model quantitatively matches the experimental data quantitatively. The deviations in the range of $0.3 < \tilde{x}_{Zn,feed2} < 0.7$ are a result of the similar lattices of aurichalcite and hydrozincite which prevents a reliable differentiation in the Rietveld refinement.[32] The quantitative data of the experiments are therefore to be evaluated critically.

In summary, the newly determined solubility products of zincian georgeite, (zincian) malachite, aurichalcite, and hydrozincite were successfully applied in the modeling of both the precipitation and the aging step in the preparation of Cu/Zn based catalysts. Furthermore, the data from our titration studies enhance the quality of the model, especially the simulation of temperature effects.

5. CONCLUSIONS

In this work, we developed an easily applicable method for the determination of solubility products for synthetic precipitate phases as a function of the temperature and elemental composition. It is meant to be used complementary to the established and highly precise, yet time-consuming, and analytically complex methods. Our method is based on easy to execute titration studies and a thermodynamic equilibrium model which comprises the solid−liquid equilibria, the speciation equilibria in the liquid phase, and activity coefficient models. Adequate software for solving these systems of equations, such as PHREEQC, is freely available. By iteration, the solubility products $K_{SP,j}$ of selected solid phases j are varied to minimize the error between calculated and measured pH. Prerequisites for the developed procedure are that the speciation equilibria of the solids forming ions involve OH^- and or H_3O^+ ions so that the pH during titration is influenced by the solids formation and that the speciation equilibria as well as activity coefficients are known precisely.

The applicability of the approach was verified with the preparation of Ni/Mn based precursors for the cathode active material (PCAM). Titration studies for $Mn(OH)_2$ confirmed solubility products found in the literature. However, for $Ni(OH)_2$ our approach revealed that significant amounts of sulfur of up to $x_S = 4.2$ wt % are incorporated into the lattice during precipitation. Especially when the precipitation is limited by the amount of available OH^- ions in the solution, the use of $K_{SP,j}$ from the literature alone could not accommodate the solids formation. Only the implementation of $Ni_8(OH)_{14}SO_4$ as an additional phase and the determination of its solubility product $[\log(K_{SP,Ni_8(OH)_{14}SO_4}/(mol^{23}·L^{-23})) = -104.2]$ enabled the modeling of the experimental titration curve. Subsequent co-precipitation studies confirmed the need for the implementation of separate $Ni(OH)_2$ and $Mn(OH)_2$ phases in the thermodynamic modeling of the process and reaffirmed the necessity to consider hydroxy-sulfate phases for Ni. By including the previously characterized hydroxy-sulfate phases into the database, we were able to quantitatively predict the amount of incorporated sulfate in PCAM with a thermodynamic equilibrium model alone.

As a second example, to verify the generality of our approach, we considered the precipitation of Cu/Zn based catalyst precursors. Here, the substitution of Cu with Zn in the amorphous precursor phase (zincian) georgeite ($[Cu,Zn]_2CO_3(OH)_2$) is targeted in the preparation at, in general, 50−80 °C. However, $K_{SP,j}$ are only available for 25 °C and for the similar crystalline phases malachite ($Cu_2CO_3(OH)_2$) and rosasite ($Cu_{1.16}Zn_{0.84}CO_3(OH)_2$), which form from the amorphous precursor phase by aging. Thus, we determined solubility products for the synthetic precursor phase zincian georgeite as a function of the temperature and its Zn fraction. Furthermore, temperature-dependent $K_{SP,j}$ for the relevant aging products aurichalcite, hydrozincite and (zincian) malachite were determined. The data significantly differ from the previously available data for the minerals. This is also evident in the co-precipitation studies conducted, where the newly determined solubility products for zincian georgeite improved the prediction of the solid mass. In separate aging studies the quantitative phase composition of the aged catalyst precursor was correctly modeled as a function of temperature and the reactant ratio by applying the new temperature-dependent $K_{SP,j}$ for the crystalline phases.

On the basis of these results, we can confirm the applicability of our new method to determine missing $K_{\mathrm{SP},j}$ from titration curves even for complex, industrially relevant precipitate phases. Furthermore, the discussed application studies prove the validity of the thus determined solubility products for process modeling. We believe that the simplicity of the suggested approach to determine solubility products can help to enhance thermodynamically based precipitation models. In particular, processes with synthetic precipitates that strongly deviate from the elemental composition or crystallinity of well-characterized mineral phases or regarding the process temperature could benefit from the new method. The two prerequisites for the transfer to other substances are that pH is affected by the solid formation and that the speciation in the liquid phase is well characterized. Thus, the obtained values for $K_{\mathrm{SP},j}$ should ideally be used in combination with the activity coefficient model and speciation database applied in the determination of the respective solubility product. We are convinced that the presented tool will contribute to optimize precipitation processes in the future, be it from an economic point of view, regarding product properties, or to make the processes more sustainable.

ASSOCIATED CONTENT

Supporting Information

The Supporting Information is available free of charge at https://pubs.acs.org/doi/10.1021/acs.iecr.4c01616.

> SI_KSP_determination contains additional analytical data of the experimental samples and additional figures which confirm and further elaborate statements and correlations discussed in the manuscript (PDF)

AUTHOR INFORMATION

Corresponding Authors

David Guse − *Institute of Thermal Process Engineering (TVT), Karlsruhe Institute of Technology (KIT), 76131 Karlsruhe, Germany;* orcid.org/0000-0001-9066-043X; Email: david.guse@kit.edu

Matthias Kind − *Institute of Thermal Process Engineering (TVT), Karlsruhe Institute of Technology (KIT), 76131 Karlsruhe, Germany;* orcid.org/0000-0002-7203-1776; Email: matthias.kind@kit.edu

Authors

Lukas Metzger − *BASF SE, 67056 Ludwigshafen, Germany*
Martin Kriesten − *BASF SE, 67056 Ludwigshafen, Germany*
Elisabeth Eiche − *Institute of Applied Geosciences (AGW), Chair of Geochemistry & Economic Geology, Karlsruhe Institute of Technology (KIT), 76131 Karlsruhe, Germany; Laboratory for Environmental and Raw Materials Analysis, Institute of Applied Geosciences, 76131 Karlsruhe, Germany*

Complete contact information is available at:
https://pubs.acs.org/10.1021/acs.iecr.4c01616

Author Contributions

The manuscript was written through contributions of all authors. All authors have given approval to the final version of the manuscript.

Notes

The authors declare no competing financial interest.

ABBREVIATIONS

CHNS, elemental analysis of C, H, N and S by F-AES; EDXS, energy-dispersive X-ray spectroscopy; F-AES, flame atomic emission spectrophotometry; FT-IR, Fourier transformed infrared spectroscopy; ICP-OES, inductively coupled plasma optical emission spectroscopy; PCAM, precursor for cathode active material; SI, supporting information; SIT, specific ion interaction theory; TEM, transmission electron microscopy; XRD, X-ray diffraction; ZG, zincian georgeite; ZM, zincian malachite

REFERENCES

(1) Arena, F.; Barbera, K.; Italiano, G.; Bonura, G.; Spadaro, L.; Frusteri, F. Synthesis, Characterization and Activity Pattern of Cu−ZnO/ZrO2 Catalysts in the Hydrogenation of Carbon Dioxide to Methanol. *J. Catal.* **2007**, *249* (2), 185−194.

(2) Pimenta, V.; Sathiya, M.; Batuk, D.; Abakumov, A. M.; Giaume, D.; Cassaignon, S.; Larcher, D.; Tarascon, J.-M. Synthesis of Li-Rich NMC: A Comprehensive Study. *Chem. Mater.* **2017**, *29* (23), 9923−9936.

(3) Malik, M.; Chan, K. H.; Azimi, G. Review on the Synthesis of LiNixMnyCo1-x-yO2 (NMC) Cathodes for Lithium-Ion Batteries. *Mater. Today Energy* **2022**, *28*, 101066.

(4) Acharjee, N.; Ganguly, S. K.; Sarangi, B.; Srivastava, A. K. A Review of Various Ceramic Pigment Preparation and Characterization Methodologies for Applications. *J. Aust. Ceram. Soc.* **2023**, *59* (2), 303−323.

(5) Lytle, D. A.; Wahman, D.; Schock, M. R.; Nadagouda, M.; Harmon, S.; Webster, K.; Botkins, J. Georgeite: A Rare Copper Mineral with Important Drinking Water Implications. *Chem. Eng. J.* **2019**, *355*, 1−10.

(6) Idroes, R.; Yusuf, M.; Alatas, M.; Subhan; Lala, A.; Saiful; Suhendra, R.; Idroes, G. M.; Marwan. Geochemistry of Hot Springs in the Ie Seu'um Hydrothermal Areas at Aceh Besar District, Indonesia. *IOP Conf. Ser. Mater. Sci. Eng.* **2018**, *334* (1), 012002.

(7) *Innovation Outlook: Renewable Methanol*; Irena And Methanol Institute, International Renewable Energy Agency: Abu Dhabi, 2021.

(8) *Production of Methanol Worldwide from 2017 to 2022*, 2022. https://www.statista.com/statistics/1323406/methanol-production-worldwide/ (accessed March 20, 2024).

(9) Pillot, C. *The Rechargeable Battery Market and Main Trends 2020−2030*, 2021. https://www.avicenne.com/pdf/The%20Rechargeable%20Battery%20Market%20and%20Main%20Trends%202020%20%E2%80%93%202030%20C%20Pillot%20Presentation%20at%20BATTERIES%202021%20Lyon%20France%20September%202021.pdf (accessed March 20, 2024).

(10) Güldenpfennig, A.; Pflug, L.; Peukert, W. How to Estimate Material Parameters for Multiphase, Multicomponent Precipitation Modeling. *Cryst. Growth Des.* **2019**, *19* (5), 2785−2793.

(11) Rehage, H.; Orthey, J.; Kind, M. On the Complete Similitude of Technical Precipitation. Part I: Impinging Mixers. *Chem. Eng. J.* **2021**, *415*, 129047.

(12) Schikarski, T.; Avila, M.; Trzenschiok, H.; Güldenpfennig, A.; Peukert, W. Quantitative Modeling of Precipitation Processes. *Chem. Eng. J.* **2022**, *444*, 136195.

(13) Clever, H. L.; Johnston, F. J. The Solubility of Some Sparingly Soluble Lead Salts: An Evaluation of the Solubility in Water and Aqueous Electrolyte Solution. *J. Phys. Chem. Ref. Data* **1980**, *9* (3), 751−784.

(14) Yoder, C. H.; Bushong, E.; Liu, X.; Weidner, V.; McWilliams, P.; Martin, K.; Lorgunpai, J.; Haller, J.; Schaeffer, R. W. The Synthesis and Solubility of the Copper Hydroxyl Nitrates: Gerhardtite, Rouaite and Likasite. *Mineral. Mag.* **2010**, *74* (3), 433−440.

(15) Alwan, A. K.; Thomas, J. H.; Williams, P. A. Mineral Formation from Aqueous Solution. Part III. The Stability of Aurichalcite, (Zn,Cu)5(CO3)2(OH)6, and Rosasite (Cu,Zn)2(CO3)(OH)2. *Transit. Met. Chem.* **1980**, *5* (1), 3−5.

(16) Bénézeth, P.; Berninger, U.-N.; Bovet, N.; Schott, J.; Oelkers, E. H. Experimental Determination of the Solubility Product of Dolomite at 50−253 °C. *Geochim. Cosmochim. Acta* **2018**, *224*, 262−275.

(17) Giffaut, E.; Grivé, M.; Blanc, Ph.; Vieillard, Ph.; Colàs, E.; Gailhanou, H.; Gaboreau, S.; Marty, N.; Madé, B.; Duro, L. Andra Thermodynamic Database for Performance Assessment: ThermoChimie. *Appl. Geochem.* **2014**, *49*, 225−236.

(18) Mattigod, S. V.; Rai, D.; Felmy, A. R.; Rao, L. Solubility and Solubility Product of Crystalline Ni(OH)2. *J. Solution Chem.* **1997**, *26* (4), 391−403.

(19) Para, M. L.; Alidoost, M.; Shiea, M.; Boccardo, G.; Buffo, A.; Barresi, A. A.; Marchisio, D. A Modelling and Experimental Study on the Co-Precipitation of Ni0.8Mn0.1Co0.1(OH)2 as Precursor for Battery Cathodes. *Chem. Eng. Sci.* **2022**, *254*, 117634.

(20) Mugumya, J. H.; Rasche, M. L.; Rafferty, R. F.; Patel, A.; Mallick, S.; Mou, M.; Bobb, J. A.; Gupta, R. B.; Jiang, M. Synthesis and Theoretical Modeling of Suitable Co-Precipitation Conditions for Producing NMC111 Cathode Material for Lithium-Ion Batteries. *Energy Fuels* **2022**, *36* (19), 12261−12270.

(21) Hartig, M. A. J.; Jacobsen, N.; Peukert, W. Multi-Component and Multi-Phase Population Balance Model: The Case of Georgeite Formation as Methanol Catalyst Precursor Phase. *Chem. Eng. Sci.* **2014**, *109*, 158−170.

(22) van Bommel, A.; Dahn, J. R. Analysis of the Growth Mechanism of Co-precipitated Spherical and Dense Nickel, Manganese, and Cobalt-Containing Hydroxides in the Presence of Aqueous Ammonia. *Chem. Mater.* **2009**, *21* (8), 1500−1503.

(23) Liang, L.; Du, K.; Peng, Z.; Cao, Y.; Duan, J.; Jiang, J.; Hu, G. Co−Precipitation Synthesis of Ni0.6Co0.2Mn0.2(OH)2 Precursor and Characterization of LiNi0.6Co0.2Mn0.2O2 Cathode Material for Secondary Lithium Batteries. *Electrochim. Acta* **2014**, *130*, 82−89.

(24) Berk, R. B.; Beierling, T.; Metzger, L.; Gasteiger, H. A. Investigation of the Particle Formation Mechanism during Co-precipitation of Ni-Rich Hydroxide Precursor for Li-Ion Cathode Active Material. *J. Electrochem. Soc.* **2023**, *170* (11), 110513.

(25) Pollard, A. M.; Spencer, M. S.; Thomas, R. G.; Williams, P. A.; Holt, J.; Jennings, J. R. Georgeite and Azurite as Precursors in the Preparation of Co-Precipitated Copper/Zinc Oxide Catalysts. *Appl. Catal. Gen.* **1992**, *85* (1), 1−11.

(26) Guse, D.; Polierer, S.; Wild, S.; Pitter, S.; Kind, M. Improved Preparation of Cu/Zn-Based Catalysts by Well-Defined Conditions of Co-Precipitation and Aging. *Chem. Ing. Technol.* **2022**, *94* (3), 314−327.

(27) Jouanneau, S.; Eberman, K. W.; Krause, L. J.; Dahn, J. R. Synthesis, Characterization, and Electrochemical Behavior of Improved Li[Ni[sub x]Co[sub 1−2x]Mn[sub x]]O[sub 2] (0.1≤x≤0.5). *J. Electrochem. Soc.* **2003**, *150* (12), A1637.

(28) Kim, K. J.; Jo, Y. N.; Lee, W. J.; Subburaj, T.; Prasanna, K.; Lee, C. W. Effects of Inorganic Salts on the Morphological, Structural, and Electrochemical Properties of Prepared Nickel-Rich Li-[Ni0.6Co0.2Mn0.2]O2. *J. Power Sources* **2014**, *268*, 349−355.

(29) Cornu, D.; Coustel, R.; Durand, P.; Carteret, C.; Ruby, C. How Can pH Drop While Adding NaOH? Formation and Transformation of Mn4(OH)6SO4. *J. Solid State Chem.* **2022**, *305*, 122631.

(30) Behrens, M.; Girgsdies, F. Structural Effects of Cu/Zn Substitution in the Malachite-Rosasite System. *Z. Für Anorg. Allg. Chem.* **2010**, *636* (6), 919−927.

(31) Behrens, M.; Girgsdies, F.; Trunschke, A.; Schlögl, R. Minerals as Model Compounds for Cu/ZnO Catalyst Precursors: Structural and Thermal Properties and IR Spectra of Mineral and Synthetic (Zincian) Malachite, Rosasite and Aurichalcite and a Catalyst Precursor Mixture. *Eur. J. Inorg. Chem.* **2009**, *2009* (10), 1347−1357.

(32) Guse, D.; Warmuth, L.; Kreißig, F.; Pitter, S.; Kind, M. *Preparation of Cu/Zn Based Catalyst Precursors—Importance of Thermodynamics and Seeding*; Deutsche Wissenschaftliche Gesellschaft für Erdöl, Erdgas und Kohle e.V. (DGMK), 2022.

(33) Pankow, J. F. *Aquatic Chemistry Concepts*, 2nd ed.; CRC Press: Boca Raton, 2019.

(34) Samson, E.; Lemaire, G.; Marchand, J.; Beaudoin, J. J. Modeling Chemical Activity Effects in Strong Ionic Solutions. *Comput. Mater. Sci.* **1999**, *15* (3), 285−294.

(35) Taylor, P. *Solubility and Stability of Inorganic Carbonates*; Atomic Energy of Canada Ltd., 1987. https://inis.iaea.org/search/search.aspx?orig_q=rn:20062977 (accessed 28 June 2024).

(36) Behrens, M.; Schlögl, R. How to Prepare a Good Cu/ZnO Catalyst or the Role of Solid State Chemistry for the Synthesis of Nanostructured Catalysts. *Z. Für Anorg. Allg. Chem.* **2013**, *639* (15), 2683−2695.

(37) Baltes, C.; Vukojevic, S.; Schuth, F. Correlations between Synthesis, Precursor, and Catalyst Structure and Activity of a Large Set of CuO/ZnO/Al2O3 Catalysts for Methanol Synthesis. *J. Catal.* **2008**, *258* (2), 334−344.

(38) Li, J.-L.; Inui, T. Characterization of Precursors of Methanol Synthesis Catalysts, Copper/Zinc/Aluminum Oxides, Precipitated at Different pHs and Temperatures. *Appl. Catal. Gen.* **1996**, *137* (1), 105−117.

(39) Martell, A. E.; Smith, R. M. *NIST Standard Reference Database 46 Version 8.0*; NIST, 2004. https://www.nist.gov/srd/nist46 (accessed 28 June 2024).

(40) Lange, N. A. *Lange's Handbook of Chemistry, McGraw-Hill Handbooks*, 15th ed.; Dean, J. A., Ed.; McGraw-Hill Education: New York, NY, 1999.

(41) Powell, K. J.; Brown, P. L.; Byrne, R. H.; Gajda, T.; Hefter, G.; Sjöberg, S.; Wanner, H. Chemical Speciation of Environmentally Significant Metals with Inorganic Ligands Part 2: The Cu2+-OH-Cl-CO32-SO42-and PO43- Systems (IUPAC Technical Report). *Pure Appl. Chem.* **2007**, *79* (5), 895−950.

(42) Haderlein, M.; Güldenpfennig, A.; Segets, D.; Peukert, W. A. A widely applicable tool for modeling precipitation processes. *Comput. Chem. Eng.* **2017**, *98*, 197−208.

(43) Preis, W.; Gamsjäger, H. Solid + Solute) Phase Equilibria in Aqueous Solution. XIII. Thermodynamic Properties of Hydrozincite and Predominance Diagrams for (Zn2++ H2O+ CO2). *J. Chem. Thermodyn.* **2001**, *33* (7), 803−819.

(44) Parkhurst, D. L.; Appelo, C. A. J. *Description of Input and Examples for PHREEQC Version 3: A Computer Program for Speciation, Batch-Reaction, One-Dimensional Transport, and Inverse Geochemical Calculations; 6-A43*; U.S. Geological Survey, 2013.

(45) Lee, M.-H.; Kang, Y.-J.; Myung, S.-T.; Sun, Y.-K. Synthetic Optimization of Li[Ni1/3Co1/3Mn1/3]O2 via Co-Precipitation. *Electrochim. Acta* **2004**, *50* (4), 939−948.

(46) Zhang, S. Characterization of High Tap Density Li[Ni1/3Co1/3Mn1/3]O2 Cathode Material Synthesized via Hydroxide Co-Precipitation. *Electrochim. Acta* **2007**, *52* (25), 7337−7342.

(47) Kim, H.; Kim, M. G.; Jeong, H. Y.; Nam, H.; Cho, J. A New Coating Method for Alleviating Surface Degradation of LiNi0.6-Co0.2Mn0.2O2 Cathode Material: Nanoscale Surface Treatment of Primary Particles. *Nano Lett.* **2015**, *15* (3), 2111−2119.

(48) Sun, Y.-K.; Chen, Z.; Noh, H.-J.; Lee, D.-J.; Jung, H.-G.; Ren, Y.; Wang, S.; Yoon, C. S.; Myung, S.-T.; Amine, K. Nanostructured High-Energy Cathode Materials for Advanced Lithium Batteries. *Nat. Mater.* **2012**, *11* (11), 942−947.

(49) Hartig, M. A. J.; Peukert, W.; Jacobsen, N.; Leuthold, A. A Model-Based Precipitation Study of Copper-Based Catalysts. *AIChE J.* **2015**, *61* (7), 2104−2116.

(50) Muhamad, E. N.; Irmawati, R.; Taufiq-Yap, Y. H.; Abdullah, A. H.; Kniep, B. L.; Girgsdies, F.; Ressler, T. Comparative Study of Cu/ZnO Catalysts Derived from Different Precursors as a Function of Aging. *Catal. Today* **2008**, *131* (1−4), 118−124.

(51) Zhang, Q.-C.; Cheng, K.-P.; Wen, L.-X.; Guo, K.; Chen, J.-F. A Study on the Precipitating and Aging Processes of CuO/ZnO/Al 2 O 3 Catalysts Synthesized in Micro-Impinging Stream Reactors. *RSC Adv.* **2016**, *6* (40), 33611−33621.

(52) Smith, P. J.; Kondrat, S. A.; Chater, P. A.; Yeo, B. R.; Shaw, G. M.; Lu, L.; Bartley, J. K.; Taylor, S. H.; Spencer, M. S.; Kiely, C. J.; Kelly, G. J.; Park, C. W.; Hutchings, G. J. A New Class of Cu/ZnO Catalysts Derived from Zincian Georgeite Precursors Prepared by Co-Precipitation. *Chem. Sci.* **2017**, *8* (3), 2436−2447.

(53) Frei, E.; Schaadt, A.; Ludwig, T.; Hillebrecht, H.; Krossing, I. The Influence of the Precipitation/Ageing Temperature on a Cu/ZnO/ZrO 2 Catalyst for Methanol Synthesis from H 2 and CO 2. *ChemCatChem* **2014**, *6* (6), 1721−1730.

(54) Charlton, S. R.; Parkhurst, D. L. Modules Based on the Geochemical Model PHREEQC for Use in Scripting and Programming Languages. *Comput. Geosci.* **2011**, *37* (10), 1653−1663.

(55) Gaines, R. V.; Skinner, H. C. W.; Foord, E. E.; Mason, B.; Rosenzweig, A. *Dana's New Mineralogy: The System of Mineralogy of James Dwight Dana and Edward Salisbury Dana*, 8th ed.; Wiley-Interscience: New York, 1997.

(56) Fan, Y.; Hua Li, G.; Yang, L.; Ming Zhang, Z.; Chen, Y.; You Song, T.; Hua Feng, S. Synthesis, Crystal Structure, and Magnetic Properties of a Three-Dimensional Hydroxide Sulfate: Mn5(OH)-8SO4. *Eur. J. Inorg. Chem.* **2005**, *2005* (16), 3359−3364.

(57) Zhao, H.; Wu, H.; Hu, H.; Li, Y.; Li, J.; Zhang, X. Cooperative Decomposition of Hydrogen Peroxide by Lignin-Combined Transition Metals in Pulp Bleaching. *BioResources* **2018**, *13* (2), 3922−3931.

(58) Puigdomènech, I.; Colàs, E.; Grivé, M.; Campos, I.; García, D. A Tool to Draw Chemical Equilibrium Diagrams Using SIT: Applications to Geochemical Systems and Radionuclide Solubility. *MRS Proc.* **2014**, *1665*, 111−116.

(59) Brown, D. S.; Allison, J. D. *MINTEQA1. An Equilibrium Metal Speciation Model*, 1987.

(60) Bridge, P. J.; Just, J.; Hey, M. H. Georgeite, a New Amorphous Copper Carbonate from the Carr Boyd Mine, Western Australia. *Mineral. Mag.* **1979**, *43* (325), 97−98.

(61) Kondrat, S. A.; Smith, P. J.; Wells, P. P.; Chater, P. A.; Carter, J. H.; Morgan, D. J.; Fiordaliso, E. M.; Wagner, J. B.; Davies, T. E.; Lu, L.; Bartley, J. K.; Taylor, S. H.; Spencer, M. S.; Kiely, C. J.; Kelly, G. J.; Park, C. W.; Rosseinsky, M. J.; Hutchings, G. J. Stable Amorphous Georgeite as a Precursor to a High-Activity Catalyst. *Nature* **2016**, *531* (7592), 83−87.

(62) Spencer, M. S. Precursors of Copper/Zinc Oxide Catalysts. *Catal. Lett.* **2000**, *66* (4), 255−257.